Evolution of hydrothermal regime along a crustal shear zone, Tinos island, Greece

Vincent Famin, P. Philippot, Laurent Jolivet, Philippe Agard

Evolution of hydrothermal regime along a crustal shear zone, Tinos Island, Greece

V. Famin[1]

Laboratoire de Tectonique, Université Pierre et Marie Curie, Paris, France

P. Philippot

CNRS, Laboratoire de Géosciences Marines, Institut de Physique du Globe, Paris, France

L. Jolivet and P. Agard

Laboratoire de Tectonique, Université Pierre et Marie Curie, Paris, France

Received 31 January 2003; revised 15 May 2004; accepted 29 June 2004; published 11 September 2004.

[1] Structural cathodoluminescence and SIMS $\delta^{18}O$ analyses of quartz-calcite veins are combined to constrain the evolution in space and time of fluid infiltration in an exhuming detachment shear zone (Tinos Island, Cyclades, Greece). Careful description of vein arrays shows that the plumbing system evolved into an interconnected network just beneath the ductile-to-brittle transition. Microtextures of quartz and calcite infilling veins display deformed relics and newly precipitated grains. High-resolution $\delta^{18}O$ mapping in relics yields a steady quartz-calcite fractionation of 2 ‰ at ~400°C, whereas fractionation increases in neograins from 2 to 5 ‰ in 190 m toward the fault, or a ~150°C temperature fall. Cooling is associated with a shift of fluid stable isotope signature from 15 ‰ to 0 ‰ beneath the detachment. Results are interpreted as advective removal of heat by massive infiltration of surface-derived fluids over depths of 10–15 km. Fluid penetration was promoted by the coalescence of late ductile-early brittle veins, as the exhuming footwall crossed the ductile-brittle transition. Only small amounts of fluids penetrated the ductile crust beneath the transitional rheology. *INDEX TERMS:* 8045 Structural Geology: Role of fluids; 8109 Tectonophysics: Continental tectonics—extensional (0905); 5114 Physical Properties of Rocks: Permeability and porosity; 8135 Tectonophysics: Hydrothermal systems (8424); 8130 Tectonophysics: Heat generation and transport; *KEYWORDS:* detachment fault, metamorphic veins, fluid flow, brittle-ductile transition, oxygen isotope thermometry, ion microprobe. **Citation:** Famin, V., P. Philippot, L. Jolivet, and P. Agard (2004), Evolution of hydrothermal regime along a crustal shear zone, Tinos Island, Greece, *Tectonics*, *23*, TC5004, doi:10.1029/2003TC001509.

1. Introduction

[2] Much attention has so far been paid to the structural and isotopic evidences for fluid-rock interactions associated to the development of metamorphic core complexes. Core complexes are exhumed by lithospheric-scale, extensional ductile shear zones which evolved into low-angle detachment faults (<30°). Evidence for large-scale mobility of trace elements and isotopes in exhumed shear zones has led to the conclusion that mylonitic rocks have interacted many times with their own weight of exotic fluids during ductile deformation [*Dipple et al.*, 1990; *Kerrich et al.*, 1984]. The ubiquitous recognition of fluid-rock interactions in detachments raises a paradox, because downward fluid flow is expected to stop at the brittle-to-ductile rheological transition in the middle crust, due to the increase of pore pressure gradient from hydrostatic to lithostatic state [*Etheridge et al.*, 1983]. Some studies have therefore favored the concept that downward fluid penetration is only restricted to the upper brittle section of detachments [*Morrison*, 1994], and that transient release of deeply seated magmatic or metamorphic fluids are responsible for the metasomatism associated to ductile shear [*Axen et al.*, 2001; *Peters and Wickham*, 1995]. In some cases, however, superficial fluids have been traced down to 10–15 km depths, well into the ductile portion of detachments [*Fricke et al.*, 1992; *Kerrich and Rehrig*, 1987], and accounted for by deformation-assisted fluid pumping [*McCaig*, 1988; *Reynolds and Lister*, 1987].

[3] The infiltration of fluids can greatly alter the strength envelope of rocks in faults, by increasing the pore pressure [*Rice*, 1992] or promoting strain softening alteration reactions [*Wintsch et al.*, 1995]. *Morrison and Anderson* [1998] have documented that fluid circulation could also dramatically cool down the sheared rocks by advective heat extraction. Knowing the source, temperature and flow mechanism of fluids during exhumation is therefore crucial to understand how detachments initiate

[1]Also at CNRS, Laboratoire de Géosciences Marines, Institut de Physique du Globe de Paris, Paris, France.

0278-7407/04/2003TC001509$12.00

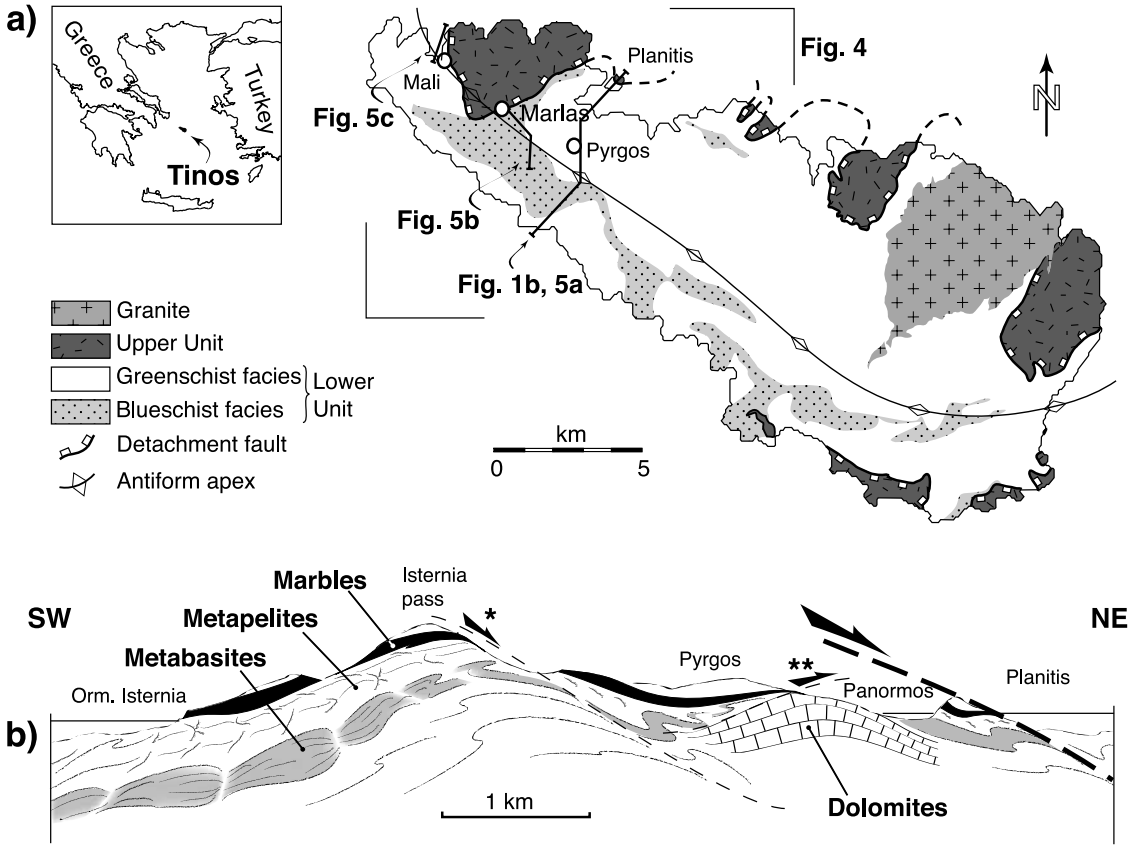

Figure 1. (a) Simplified geological map of Tinos Island [after *Mélidonis*, 1980]. (b) Simplified SW-NE cross section from Ormos-Isternia to Planitis Islet, showing the evolution of ductile deformation toward the detachment on the NE side of the core complex antiform. The single asterisk marks the secondary shear zone proposed by *Parra et al.* [2002]. The double asterisk marks the thrust fault proposed by *Avigad and Garfunkel* [1989] for the emplacement of dolomite marbles.

and slip at low angle, and how fluids participate to the slip. Most studies, however, have provided information on the final pattern of fluid-deformation interactions, but not on the evolution of the plumbing system in space and time. This paper uses a variety of field and analytical approaches to constrain the simultaneous evolution of deformation and fluid penetration in the footwall of a detachment fault on the example of Tinos Island (Cyclades, Greece). We combine detailed microstructural studies and cathodoluminescence imaging with ion-microprobe oxygen isotope thermometry on quartz and calcite infilling metamorphic veins, to document the temperature-deformation-infiltration history of the shear zone. These data are then used to illustrate how the shear zone evolved progressively from a low fluid flux, rock-buffered system to a strongly drained channelized open system transporting large volumes of meteoric waters.

2. Geological Settings

[4] The Aegean Sea was formed during the Tertiary at the expense of the Alpine belt of the Hellenides [*Avigad and Garfunkel*, 1991; *Bonneau and Kienast*, 1982]. Aegean extension results from the southward retreat of the African slab below Crete, accommodating the sinistral slip of the North Anatolian Fault as a response to the overall westward extrusion and collapse of Turkey [*Angelier et al.*, 1982; *Le Pichon et al.*, 1995; *McKenzie*, 1972]. Crustal thinning has been active in the back arc region of the Hellenic trench since at least the early Miocene [*Gautier and Brun*, 1994b; *Jolivet et al.*, 1994]. The Miocene reworking of the Hellenides by extension resulted in the widespread exposure of cordilleran-type HP-LT metamorphic belts in the Cyclades [*Lister et al.*, 1984] and in the Rhodope [*Dinter and Royden*, 1993; *Sokoutis et al.*, 1993] exhumed along crustal-scale normal detachment faults [*Avigad and Garfunkel*, 1991; *Faure et al.*, 1991; *Gautier and Brun*, 1994a; *Lee and Lister*, 1992] and intruded by Miocene granitoids [*Altherr et al.*, 1982; *Dürr et al.*, 1978].

[5] This structuration is well preserved on Tinos Island (Figure 1a) [*Mélidonis*, 1980; *Avigad and Garfunkel*, 1989]. The lower unit comprises a volcano-sedimentary sequence of interbedded metabasites, metapelites and

Table 1. Summary of Veining Events and Crosscutting Relations

Vein Stage	Structural Pattern	Deformation Style	Chronological Criteria	Mineralogy
V1	synfolial lenses	ductile	Sheared by C-S structures, reworked by V2a, intersected by V2b and V3.	quartz, calcite ± mica, chlorite
V2a	synfolial boudins	late ductile	Boudinaged by ductile flow. Pressure shadows of V1, intersected by V2a.	quartz, calcite, albite, chlorite, iron carbonates ± mica, sulphides
V2b	folded joints	late ductile-early brittle	Folded by vertical shortening, crosscut V1 and V2a, intersected by V3.	quartz, calcite, albite, chlorite, iron carbonates ± mica, sulphides
V3	tension gashes	brittle	Not deformed, crosscut V1 and V2, also occurs in granite intrusions.	quartz, albite, calcite, brown chlorite, iron oxides

marbles affected by Eocene (40–45 Ma) eclogite to blueschist facies metamorphism, as a consequence of Alpine orogenesis [*Dürr et al.*, 1978]. High-pressure rocks were partly overprinted by greenschist facies assemblages during the Miocene (21–23 Ma) in response to their interaction with H_2O-rich fluids during exhumation [*Bröcker*, 1990; *Bröcker and Franz*, 1998; *Bröcker et al.*, 1993]. The metamorphic conditions of the blueschist and greenschist facies events have been estimated at about 1.2–1.5 GPa and 450°–550°C, and 0.2–0.7 GPa and 440°–470°C, respectively [*Bröcker*, 1990; *Bröcker et al.*, 1993; *Parra et al.*, 2002].

[6] The upper unit forms a dismembered ophiolite sequence [*Katzir et al.*, 1996] composed of serpentinites, metabasites and metagabbros that have experienced greenschist facies metamorphism in an oceanic environment during Late Cretaceous [*Bröcker and Franz*, 1998; *Patzak et al.*, 1994]. On the southern part of the island, both upper and lower units were intruded by two Miocene granodiorite bodies at 19 and 14 Ma [*Altherr et al.*, 1982, 1988], causing a contact metamorphism aureole of about 1 km width [*Mélidonis*, 1980].

[7] The detachment separating the two units is a sharp shallow-dipping discontinuity, presenting all the features of a major ductile extensional shear zone [*Avigad and Garfunkel*, 1991; *Gautier and Brun*, 1994a, 1994b]. The core complex nature of the lower unit is illustrated by its NW-SE elongated dome shape (Figure 1a) with stretching lineation trending NE at the regional scale [*Gautier and Brun*, 1994b; *Jolivet and Patriat*, 1999]. The distribution of ductile deformation patterns and metamorphism is strongly asymmetric on the two sides of the antiform (Figure 1b). Well-preserved blueschist facies occurrences are found only on the SW half of the island where deformation is mainly accommodated by coaxial stretching (conjugate sets of kinematic indicators), whereas fully retrogressed rocks are most abundant on the NE half where finite strain is highly noncoaxial (top to NE kinematic indicators) [*Jolivet and Patriat*, 1999]). Retrogression is maximum in the ~20-m-thick talc-mylonite zone underlying the detachment. The degree of greenschist facies overprint is thus correlated with the amount of simple shear deformation observable in the field [*Gautier and Brun*, 1994a; *Jolivet and Patriat*, 1999]. These facts suggest that the shear zone evolved from a nonlocalized shear in the deep crust during the Eocene, to a strongly localized conduit for fluid migration between 19 and 23 Ma, at midcrustal conditions (10–15 km, 400°–450°C), close to depth of the so-called ductile-to-brittle transition.

3. Metamorphic Veins

[8] As a consequence of strain regime evolution, vein occurrences and fabrics are asymmetric on the two sides of the dome antiform. Three main generations of metamorphic veins, formed at different stages of the exhumation history were recognized in this study (Table 1). Structures are summarized in Figure 2.

3.1. Ductile Veins

[9] Type I vein (V1) consists of synfolial lenses of various dimensions (centimeter to meter; Figure 3a), pressure shadows developing around boudins and porphyroclasts in mafic rocks, and meter-scale planar layers oriented parallel to the foliation plane. Lens-shaped pods are widespread, whereas planar layers are found only on the SW part of the island. Although present in all lithologies except dolomitic marbles, V1 is most abundant in metapelites. In all localities, V1 is crosscut by greenschist facies C-S structures or by different generations of later veins.

[10] V1 veins are mainly composed of quartz and calcite with minor amounts of white micas and chlorite. Locally, fragments of garnet, epidote and glaucophane from the wall rock have been incorporated into the vein matrix. In thin section, quartz and calcite show a bimodal grain size distribution (Figure 3b). Lens-shaped relics of coarse grains show patchy undulose extinction and elongate subgrains oriented parallel to the foliation plane. Calcite crystals have developed bent and intersected twins consistent with a temperature of deformation greater than 200°C [*Burkhard*, 1993]. Twins have a synthetic or antithetic oblique orientation with respect to the foliation. Coarse relics pass laterally into domains of small, dynamically recrystallized (sub)-grains, organized along shear planes. New grains themselves display undulose extinction, indicating further deformation after recrystallization. Mica and chlorite flakes form sigmoidal fish in the most intensely recrystallized domains. Microstructures are intersected by vertical fluid inclusion trails, nearly perpendicular to the main foliation. Macro and microstructural features show that V1 formed

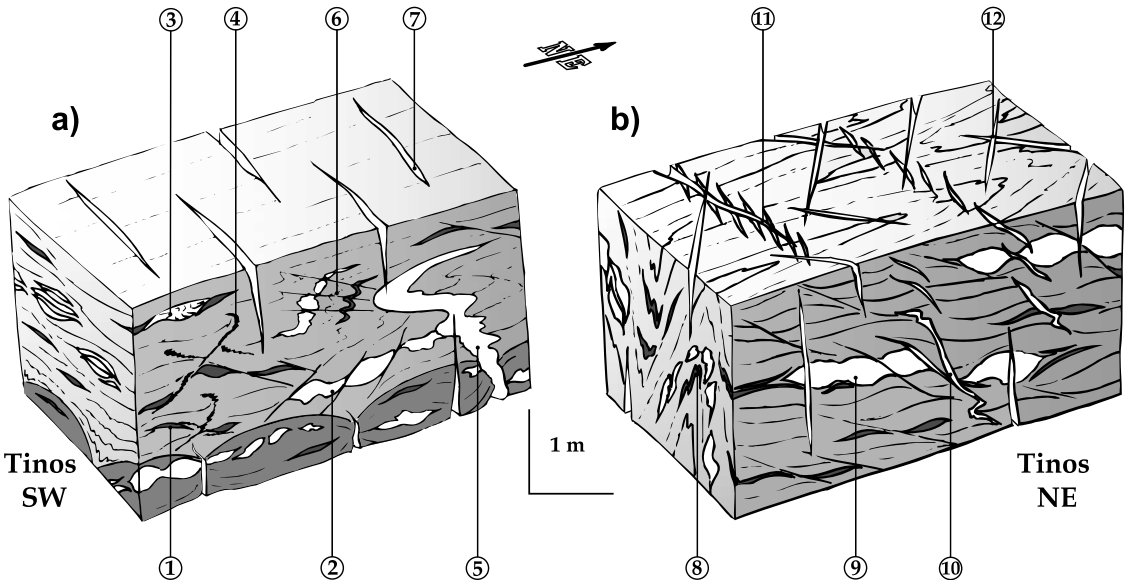

Figure 2. Synthetic sketches of veins and associated structures occurring in the lower unit on (a) the SW side of Tinos and (b) the NE side. Circled numbers indicate the following structures: 1, V1 veins reworked by ductile S-C fabrics; 2, V2a veins crosscut by top to SW S-C fabrics; 3, V2a in the pressure shadow of V1; 4, V2b veins in symmetrical steeply dipping shear planes reworking V1; 5, V2b veins, subvertical and N135°E trending in metabasites, strongly folded in metapelites; 6, crenulation cleavage developing around V2b and reworking V1 and V2a; 7, N135°E trending V3 vein; 8, V1 and V2a folded by lateral shortening perpendicular to the direction of shearing; 9, V2a reworked by top to NE sense of shear; 10, different fabrics of V2b, from steeply dipping shear planes to folded extensional joints, laterally evolving into en echelon structures; 11, N80°-N100°E V2b network connecting at high angle the N135°E population; 12, two populations of V3 oriented N-S and E-W.

during the HP-LT metamorphism or during the decompression path, and predate the general fabric of greenschist facies ductile deformation that has structured the lower unit.

3.2. Ductile-to-Brittle Veins

[11] Type 2 vein (V2) encompasses a wide range of morphologies depending on the host rock competency and the degree of ductile deformation experienced by this host. With the exception of dolomite marbles, V2 is abundant in all lithologies and most specifically in mafic rocks. V2 contains quartz, calcite, albite, chlorite and iron carbonates (ankerite, siderite) with minor amounts of white mica and sulfides (pyrite and chalcopyrite). Two main subtypes of V2 have been distinguished in the field. Subtype V2a occurs either as synfolial boudins ranging from centimetric to decametric scale, which are oriented parallel to the foliation plane (Figure 3c), or as pressure shadows developing after V1. Interestingly, V2a veins show opposite shear senses on the two sides of the island (top-to-SW on the SW of the dome, top-to-NE on the NE), suggesting a shear sense inversion on the SW due to the bulge of the dome as in the Lister and Davis model [*Lister and Davis*, 1989]. As a general observation, V2a shows a considerably less deformed fabric than V1 at the outcrop scale, with subhedral-shaped albite and carbonate crystals. Microscopically, V2a displays a subequigranular texture (Figure 3d). Quartz grains show sweeping undulose extinction, with little evidence of dynamic recrystallization. Calcite displays randomly oriented bent and intersected deformation twins (Type III of *Burkhard* [1993]). Plagioclase occurs as large subhedral grains showing deformation lamellae and microfractures filled with calcite. Large iron carbonate euhedral grains are frequently replaced in part by brown iron oxides.

[12] In contrast to V2a, subtype V2b is systematically oriented at high angle to the foliation plane (Figure 3e). V2b occurs as high-angle shear planes, en echelon cracks or decimetric to metric joints folded by vertical shortening. As these joints show different degrees of folding depending on the strength of the host rock (strongly folded in metapelites and subvertical in metabasites), no clear relative chronology was determined. Locally, V2b crosscut V2a and V1. On a regional scale, V2b is consistently oriented N135°E (Figure 4). Importantly, Figure 4 shows that another population of V2b oriented N80°–N100°E occurs in the vicinity of the detachment. This vein network is present either as an independent set or interconnecting the N135°E en echelon network without any clear chronological criteria. In thin section, mineral filling V2b are usually coarse-grained and equigranular with euhedral shapes (Figure 3f). No or little evidence of intracrystalline plastic deformation is found in

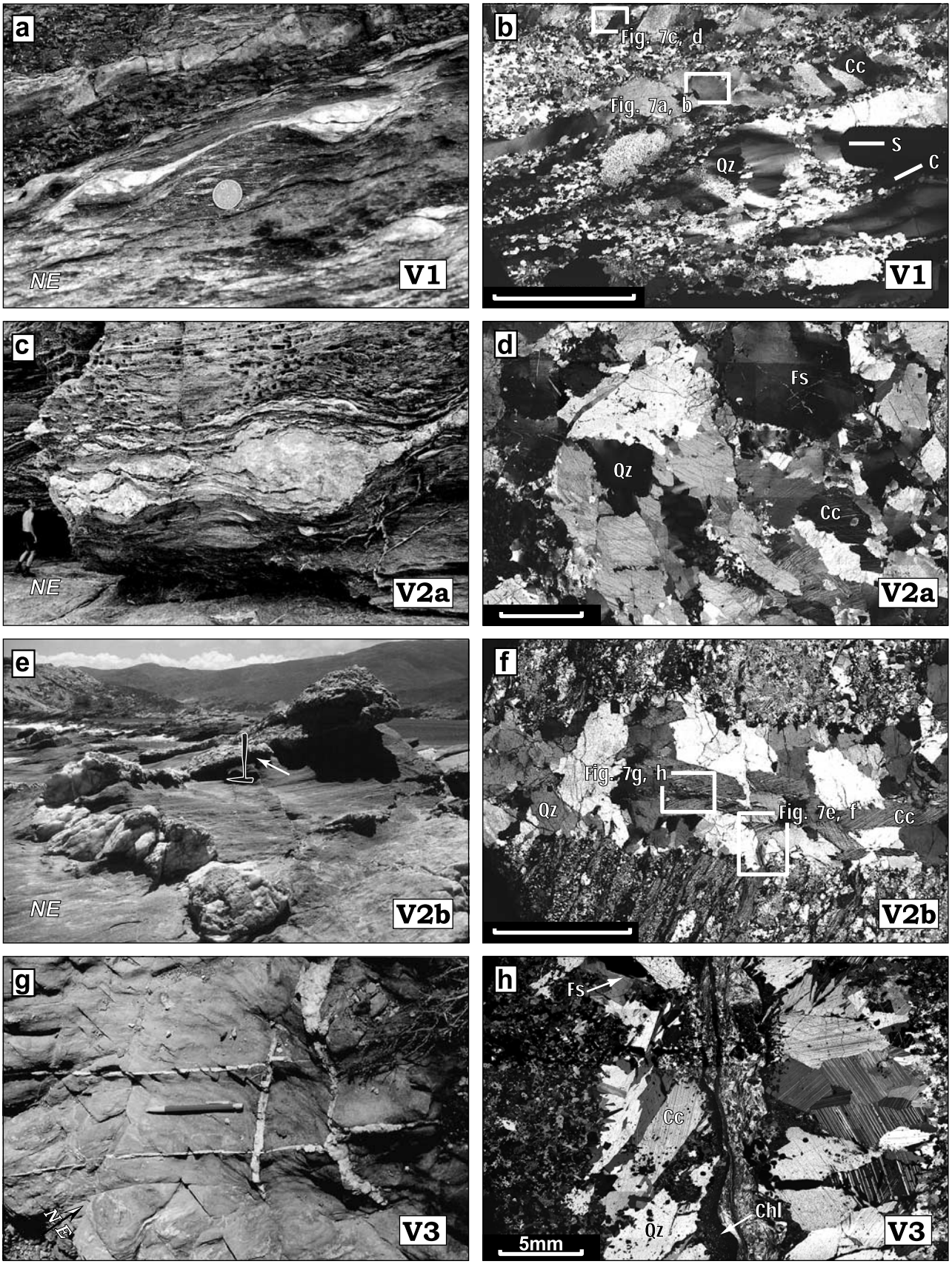
a
NE
V1
b
Fig. 7c, d
Fig. 7a, b
Cc
S
C
Qz
V1
c
NE
V2a
d
Fs
Qz
Cc
V2a
e
NE
V2b
f
Fig. 7g, h
Qz
Fig. 7e, f
Cc
V2b
g
N
E
V3
h
Fs
Cc
Chl
Qz
5mm
V3

Figure 3

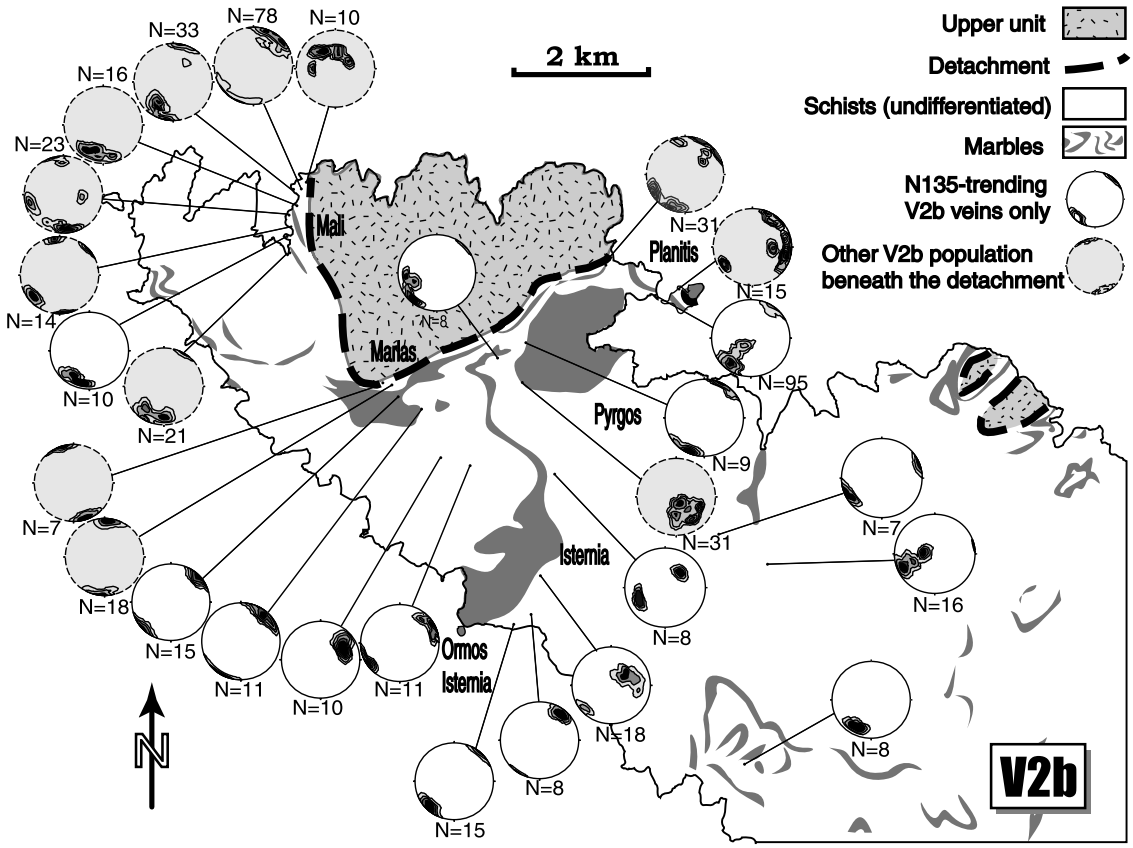

Figure 4. Stereograms of poles of V2b veins on the north of Tinos (corrected from the dip of foliation, equal area, lower hemisphere). White stereograms: N135°E trending V2b only. Gray stereograms: other population of V2b oriented N80°E to N100°E, found on the NE side of the dome when approaching the detachment, either as an independent set or interconnecting the N135°E en echelon network without any clear chronological criteria.

quartz and feldspar, while calcite may develop deformation twins consistent with temperatures in the range 150°–300°C. In contrast to the former vein types, V2b shows evidence for cataclastic deformation. Fractures and associated voids are filled with secondary quartz and calcite, showing xeno- or automorph shapes depending on the size of the voids. Fluid inclusion trails oriented parallel to the vein walls are abundant in all V2b, specifically in the vicinity of the detachment. Overall, recognition that V2 shows a large variety of different morphologies and structures ranging from quasiplastic to strictly brittle, but contains the same greenschist facies mineral assemblage, strongly suggests that the veins formed continuously during exhumation and retrograde metamorphism as the rocks were progressively carried across the ductile-to-brittle transition.

3.3. Late to Postkinematic V3 Veins

[13] Type 3 vein (V3) forms brittle extensional joints of decimetric to metric scale with moderate offsets. Two populations oriented E-W and N-S are found on a regional scale (Figure 3g). V3 contains quartz, albite, calcite, brown chlorite and oxides showing syntaxial zonation (Figure 3h). V3 affects all lithologies and existing structures throughout

Figure 3. Outcrop-scale and microscopic-scale (cross-polarized light) photographs of metamorphic veins encountered in the lower unit. (a) V1 synfolial vein showing a top to NE sense of shear. (b) Lens-shaped elongated quartz and calcite crystals with undulose extinction in V1. (c) Boudinaged V2a vein, affected by top to NE shearing. (d) Quartz grains have undulose extinction while K-feldspar crystals are fractured in V2a. Calcite display bent and intersected deformation twins. (e) Folded V2b vein intersecting the foliation plane. Open arrow marks hammer. (f) V2b microfabric is similar to V2a, with a less pronounced intracrystalline deformation. (g) V3 extensional veins open as perpendicular brittle joints. N-S vertical veins intersect E-W vertical veins with a moderate sinistral offset. (h) Syntaxial zonation in V3. Figure 6 images are localized on microphotographs.

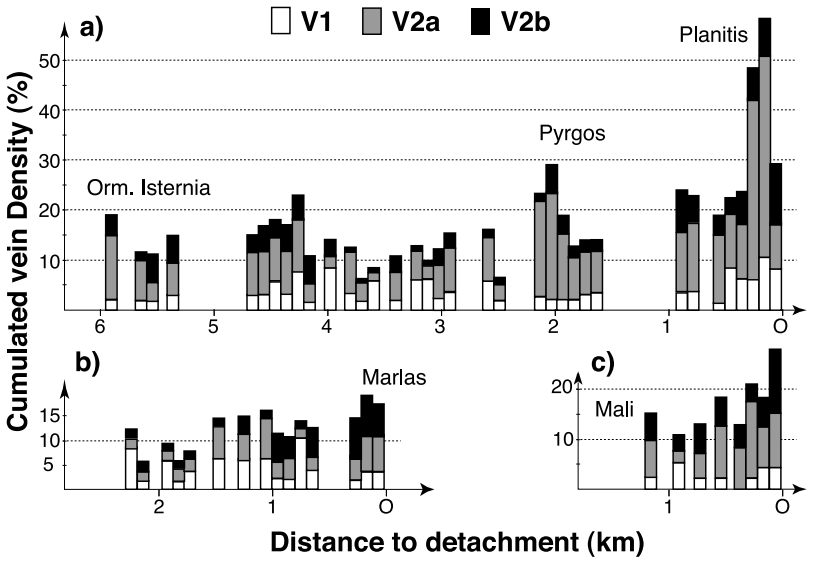

Figure 5. Evolution of cumulated vein density as a function of the distance to detachment along three SW-NE traverses, all lithologies confounded (see Figure 1a for location). Vein density was taken as the proportion of the total observable area of each vein type relative to the outcrop area. (a) Ormos-Isternia to Planitis traverse (Figure 1b). (b) Marlas traverse (c) Mali traverse. White areas, V1 veins; gray areas, V2a; black areas, V2b.

the island, including early V1 and V2 veins, dolomite marbles as well as the granitoid intrusions. V3 is interpreted to postdate the motion of the detachment fault and was not considered further here.

3.4. Vein Density

[14] The density of the different vein populations has been visually estimated at the outcrop scale along three main traverses oriented perpendicular to the detachment fault (Figure 5). These include Ormos Isternia-Planitis, Mali and Marlas (Figures 1a and 1b). Vein density was taken as the proportion of the total observable area of each vein type relative to the outcrop area. The cumulated diagrams show that the total surface area of veins increases toward the detachment. V1 density ranges between 0 and 10% along the three transects (Figure 5). No structural control other than lithologic is observed. Contrastingly, V2a density is clearly higher on the retrogressed NE side of the dome structure than on the preserved SW side. On the SW side of Tinos, V2a density clusters between 1 and 12%. In the NE side of the island, V2a density ranges between 1 and 15%, with values locally reaching 20 and 40% in metabasites at Pyrgos and Planitis, respectively (Figure 5a). V2b density ranges from less than 5% in the SW region and to more than 12% beneath the detachment in all localities (Figure 5c).

[15] Because V2b represents the latest stage of veining experienced by the detachment before brittle deformation, these veins were studied in detail for their oxygen stable isotopic composition (see below). For this reason, we estimated the cumulated frequency of V2b beneath the detachment at Planitis, Marlas and Mali. Frequency measurements were made at different spots located at increasing distances under the detachment (typically 0, 15–20, 40, 80–100 m). Cumulated frequency was defined as the number of veins counted in a spacing of n meters around a given V2b vein [*Roberts et al.*, 1999]. As shown in Figure 6, the cumulated frequency of V2b displays an n-root distribution function. For example, considering a circle of 1 m radius around a V2b vein, Figure 6a shows that at Planitis, 20 veins are counted in this surface at 80 m from the detachment, 30 veins at 40 m, 35 veins at 15 m and 45 veins at the contact. A similar marked increase in cumulated frequencies of V2b approaching the contact has been recognized at Marlas (Figure 6b, the lack of data at 0 m from the contact for spacing greater than 100 cm being due to the poor exposure of the outcrop). With regards to Mali, despite recognition of a marked increase of the concentration of V2b near the detachment, Figure 6c shows that the V2b cumulated frequencies vary independently of the distance to the detachment. This suggests that the V2b network is more homogeneously distributed at this locality than at Marlas and Planitis. Note that the density increase and vein spacing decrease of V2b (Figures 5, 6), combined with the presence of second population of V2b veins beneath the detachment (Figure 4) suggest that V2b form an interconnected network of channel ways in the vicinity of the contact at the end of ductile deformation history.

4. Methodology

4.1. Sampling Strategy

[16] Samples for this study were taken in interlayered greenschist facies mylonites, metapelites, and metacarbonates at Mali, along a single traverse 200 m in length oriented

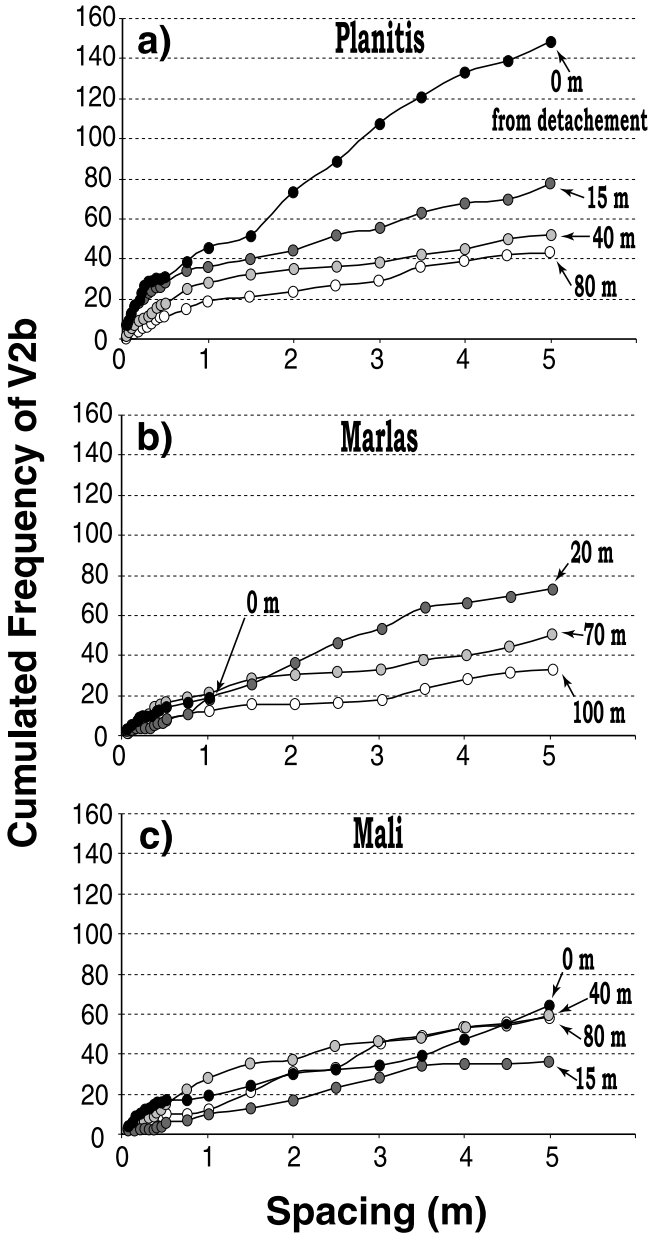

Figure 6. Cumulated frequencies of V2b veins as a function of the distance below the detachment. Cumulated frequency was defined as the number of veins counted in a spacing of X meters around a given V2b vein. Darkening dots mark the measurements made at decreasing distance under the detachment. (a) Planitis Island. (b) Marlas. (c) Mali.

perpendicular to the detachment (Figure 8a). All the different stages of the ductile and brittle deformation history are recorded by V1 and V2b veins as will be explained below, so we chose to perform oxygen isotopic analysis on the following samples: V2b.1 (1 m under the fault), V2b.2 (3 m), V1.1 and V2b.3 (8 m), V2b.4 (12 m), V2b.5 (20 m), V1.2 and V2b.6 (45 m), V1.3 and V2b.7 (60 m), V1.4 and V2b.8 (80 m), V2b.9 (200 m). In addition, a V1 sample (V1.5) from a well-preserved blueschist metacarbonate located at about 200 m beneath the detachment at Marlas was taken as a reference value unaltered by fluid infiltration attending greenschist facies metamorphism.

4.2. Cathodoluminescence

[17] All samples were examined in thin section using optical microscopy and cathodoluminescence (CL) in order to establish a relative chronology of crystallization of quartz-calcite pairs, and to identify zones where the two minerals are most likely to be in isotopic equilibrium. CL imaging was performed on a Technosyn Mark II cold-cathode device mounted on a Nikon Optiphot microscope, using a 15 kV accelerating voltage and a beam current of 0.5 mA. The resulting images were captured as microphotographs on Kodak Ektachrome P1600x photographic films.

4.3. Oxygen Isotope Composition

[18] Oxygen isotope microanalyses were performed on a Cameca IMS 1270 ion microprobe at the CRPG-CNRS (Nancy, France). Measurements were carried out in the Au-coated thin sections, on the edge of quartz grains and adjacent calcite grains displaying an equilibrium texture (see examples of $\delta^{18}O$ mapping in Figures 6b, 6d, 6f, and 6h). Ion microprobe analyses were made in three analytical sessions (29 November 2001, 01 Mars 2001, 20–21 September 2001, Table 2). Tuning and analysis were operated by the CRPG scientists, using the same procedure for the three sessions. Each Au-coated sample was sputtered with a 10 kV Cs^+ primary beam of $\sim$0.5 nA current focused to 20 $\times$ 40 μm spots. Positive charges at the samples surface were neutralized using the normal-incidence electron flood gun. Secondary O^- ions were accelerated at 10kV and analyzed at a mass resolution of $\sim$5000 using a circular focusing mode and a transfer optic of 150 μm. No interference with the ^{16}O and ^{18}O peaks occurs at this mass resolution. The position of the energy window was -25 ± 60 V, corresponding to the optimized acceptance by the spectrometers. O isotopic ratios were analyzed in multicollection mode using two off-axis Faraday cups to count simultaneously ^{16}O and ^{18}O ion intensities. The gain of the Faraday cups was calibrated at the beginning of each day session using the Cameca built-in amplifier calibration routine. Typical ion intensities of about 4.10^6 and 2.10^9 counts per second were obtained on the ^{18}O and ^{16}O peaks, yielding an internal 1σ error of $\pm$0.1 ‰ to $\pm$0.5 ‰ after a few minutes of counting (Table 2). The average external reproducibility, as estimated by replicate measurements for different spots on quartz and calcite standards, was better than $\pm$0.50 ‰ for quartz and $\pm$0.80 ‰ for calcite on each of the three analytical sessions (Table 2).

[19] Oxygen isotopic ratios were expressed as deviation relative to the Standard Mean Ocean Water reference (SMOW). The instrumental mass fractionations (IMF) were determined and monitored using quartz standards (QzCWRU, +24.52 ‰; Bogala Quartz, +12.34 ‰; Quartz Brazil, +9.60 ‰) and calcite standards (MEX, +23.64 ‰; CARB, +11.31 ‰), analyzed conventionally for O isotopes and whose homogeneity at the 20 μm scale had been demonstrated in other SIMS studies [*Aléon et al.*, 2002;

Table 2. Ion Probe $\delta^{18}O$ Data on Quartz-Calcite Pairs in V1 and V2b Veins, and Calculated Fractionations, Temperatures, and Oxygen Isotope Composition of Water

Sample	$Q_z - C_c$ Pair	$^{18}O/^{16}O$ Q_z ± 1σ, ‰	$^{18}O/^{16}O$ C_c ± 1σ, ‰	$\delta^{18}O_{Qz/SMOW}$ ± 1σ, ‰	$\delta^{18}O_{Cc/SMOW}$ ± 1σ, ‰	Δ_{Qz-Cc}, ‰	T,[a] °C	$\delta^{18}O_{H2O}$, ‰ ($Q_z - H_2O$)[b]	$\delta^{18}O_{H2O}$, ‰ ($C_c - H_2O$)[c]
29 November 2000, IMF on calcite = −10.06 ± 0.72 ‰, IMF on quartz = −11.65 ± 0.41 ‰[d]									
Mex (23. 64 ‰)	Std Cc		13.30 ± 0.26		23.36 ± 0.76				
Mex	Std Cc		13.70 ± 0.24		23.76 ± 0.75				
Mex	Std Cc		13.93 ± 0.25		23.99 ± 0.76				
Mex	Std Cc		12.78 ± 0.36		23.27 ± 0.80				
Mex	Std Cc		13.21 ± 0.16		24.87 ± 0.73				
Mex	Std Cc		14.81 ± 0.21		22.67 ± 0.75				
Mex	Std Cc		12.61 ± 0.18		23.27 ± 0.74				
Carb (11.31 ‰)	Std Cc		2.31 ± 0.32		12.37 ± 0.78				
Carb	Std Cc		0.71 ± 0.24		10.77 ± 0.75				
Carb	Std Cc		0.38 ± 0.26		10.44 ± 0.76				
Carb	Std Cc		1.22 ± 0.24		11.28 ± 0.75				
Carb	Std Cc		2.19 ± 0.18		12.25 ± 0.74				
Carb	Std Cc		1.60 ± 0.24		11.66 ± 0.75				
Carb	Std Cc		0.63 ± 0.22		10.69 ± 0.75				
QzCWRU (24.52 ‰)	Std Qz	12.72 ± 0.35		24.37 ± 0.54					
QzCWRU	Std Qz	12.58 ± 0.30		24.23 ± 0.51					
QzCWRU	Std Qz	13.48 ± 0.27		25.13 ± 0.49					
QzCWRU	Std Qz	12.51 ± 0.40		24.16 ± 0.57					
QzCWRU	Std Qz	12.93 ± 0.30		24.58 ± 0.51					
Bogala Qz (12.34 ‰)	Std Qz	1.33 ± 0.26		11.91 ± 0.48					
Bogala Qz	Std Qz	0.14 ± 0.44		12.09 ± 0.60					
Bogala Qz	Std Qz	0.77 ± 0.40		12.05 ± 0.57					
Bogala Qz	Std Qz	0.66 ± 0.30		11.95 ± 0.51					
V1.5 at 200 m	1	12.77 ± 0.27	12.67 ± 0.22	24.40 ± 0.47	22.67 ± 0.78	1.73 ± 0.91	398 ± 180	19.20 ± 4.34	19.01 ± 3.01
V1.5	1	12.43 ± 0.35	14.25 ± 0.28	24.06 ± 0.52	24.25 ± 0.8	−0.19 ± 0.95	...	...	...
V1.5	1	12.05 ± 0.33	13.48 ± 0.25	23.68 ± 0.51	23.48 ± 0.79	0.20 ± 0.94	...	...	...
V1.5	1	13.36 ± 0.31		24.99 ± 0.49					
V1.5	1	12 .23 ± 0.27		23.86 ± 0.5					
V1.5	1	12.23 ± 0.32		23.86 ± 0.47					
V1.5	1	12.52 ± 0.32		24.15 ± 0.5					
V1.5	2	13.02 ± 0.32	22.92 ± 0.27	24.65 ± 0.5	22.92 ± 0.8	1.73 ± 0.94	398 ± 186	19.45 ± 4.49	19.26 ± 3.11
V1.5	2	12.82 ± 0.40	12.15 ± 0.24	24.45 ± 0.56	22.15 ± 0.79	2.30 ± 0.97	309 ± 126	16.57 ± 4.66	16.60 ± 3.48
V1.5	2	12.19 ± 0.28	13.35 ± 0.21	23.82 ± 0.48	23.35 ± 0.77	0.47 ± 0.91	...	...	...
V1.5	2	12.08 ± 0.46	13.22 ± 0.26	23.71 ± 0.6	23.22 ± 0.79	0.49 ± 0.99	...	...	...
V1.5	2	12.69 ± 0.36	14.04 ± 0.28	24.32 ± 0.53	24.04 ± 0.8	0.28 ± 0.96	...	...	...
1 March 2001, IMF on calcite = −5.33 ± 0.78 ‰, IMF on quartz = −7.77 ± 0.48 ‰[d]									
Brazil Qz (9.60 ‰)	Std Qz	2.23 ± 0.14		10.00 ± 0.50					
Brazil Qz	Std Qz	1.10 ± 0.33		8.87 ± 0.58					
Brazil Qz	Std Qz	2.29 ± 0.18		10.06 ± 0.51					
Brazil Qz	Std Qz	1.69 ± 0.23		9.46 ± 0.53					
Brazil Qz	Std Qz	1.84 ± 0.13		9.61 ± 0.49					
Mex (23.64 ‰)	Std Cc		17.66 ± 0.27		22.99 ± 0.83				
Mex	Std Cc		17.93 ± 0.20		23.26 ± 0.81				
Mex	Std Cc		18.12 ± 0.20		23.45 ± 0.81				
Mex	Std Cc		19.10 ± 0.27		24.43 ± 0.83				
Mex	Std Cc		19.46 ± 0.21		24.79 ± 0.81				
Mex	Std Cc		17.58 ± 0.28		22.91 ± 0.83				
V1.1 at 8 m	1	12.95 ± 0.23	13.39 ± 0.21	20.72 ± 0.53	18.72 ± 0.81	2.00 ± 0.97	351 ± 154	14.26 ± 4.63	14.19 ± 3.34
V1.1	1	13.48 ± 0.20	13.94 ± 0.19	21.25 ± 0.52	19.27 ± 0.8	1.98 ± 0.95	354 ± 155	14.88 ± 4.56	14.81 ± 3.29
V1.1	2	14.83 ± 0.20	14.39 ± 0.23	22.60 ± 0.52	19.72 ± 0.81	2.88 ± 0.96	247 ± 91	12.03 ± 4.71	12.17 ± 3.70
V1.1	2	14.93 ± 0.33	14.23 ± 0.27	22.70 ± 0.58	19.56 ± 0.83	3.14 ± 1.01	225 ± 84	10.91 ± 4.97	11.06 ± 3.97
V1.1	2	15.46 ± 0.17	14.48 ± 0.28	23.23 ± 0.51	19.81 ± 0.83	3.42 ± 0.97	205 ± 72	10.13 ± 4.84	10.28 ± 3.93
V1.1	2	13.71 ± 0.24	13.01 ± 0.17	21.48 ± 0.54	18.34 ± 0.8	3.14 ± 0.97	225 ± 81	9.69 ± 4.76	9.84 ± 3.80
V1.4 at 80 m	1	12.31 ± 0.33	12.84 ± 0.21	20.08 ± 0.58	18.17 ± 0.81	1.91 ± 1.00	366 ± 170	14.05 ± 4.75	13.94 ± 3.38
V1.4	2	11.47 ± 0.23	11.73 ± 0.27	19.24 ± 0.53	17.06 ± 0.83	2.18 ± 0.98	325 ± 139	11.95 ± 4.73	11.94 ± 3.49
V1.4	2	11.42 ± 0.21	12.00 ± 0.20	19.19 ± 0.52	17.34 ± 0.82	1.85 ± 0.97	376 ± 174	13.44 ± 4.63	13.30 ± 3.27
V1.4	2	10.81 ± 0.24	11.12 ± 0.40	18.58 ± 0.54	16.45 ± 0.88	2.13 ± 1.03	332 ± 150	11.52 ± 4.94	11.50 ± 3.63
V1.2 at 45 m	1	12.59 ± 0.27	13.13 ± 0.16	20.36 ± 0.55	18.46 ± 0.8	1.90 ± 0.97	368 ± 167	14.38 ± 4.63	14.26 ± 3.29
V1.2	2	13.58 ± 0.26	13.25 ± 0.27	21.35 ± 0.55	18.58 ± 0.83	2.77 ± 1.00	258 ± 99	11.30 ± 4.85	11.42 ± 3.77
V1.2	2	13.35 ± 0.28	12.98 ± 0.21	21.12 ± 0.56	18.31 ± 0.81	2.81 ± 0.98	254 ± 96	10.88 ± 4.80	11.01 ± 3.75
V1.2	2	11.71 ± 0.22	12.00 ± 0.18	19.48 ± 0.53	17.33 ± 0.8	2.15 ± 0.96	329 ± 138	12.33 ± 4.61	12.31 ± 3.39
V1.2	2	13.30 ± 0.29	13.31 ± 0.23	21.07 ± 0.56	18.64 ± 0.81	2.43 ± 0.98	294 ± 119	12.61 ± 4.75	12.67 ± 3.59

Table 2. (continued)

Sample	$Q_z - C_c$ Pair	$^{18}O/^{16}O$ Q_z ± 1σ, ‰	$^{18}O/^{16}O$ C_c ± 1σ, ‰	$\delta^{18}O_{Qz/SMOW}$ ± 1σ, ‰	$\delta^{18}O_{Cc/SMOW}$ ± 1σ, ‰	Δ_{Qz-Cc}, ‰	T,[a] °C	$\delta^{18}O_{H2O}$, ‰ ($Q_z - H_2O$)[b]	$\delta^{18}O_{H2O}$, ‰ ($C_c - H_2O$)[c]
V1.3 at 60 m	1	15.01 ± 0.13	15.66 ± 0.19	22.78 ± 0.5	20.99 ± 0.8	1.79 ± 0.94	387 ± 177	17.30 ± 4.50	17.14 ± 3.15
V1.3	2	15.94 ± 0.21	15.97 ± 0.26	23.71 ± 0.52	21.30 ± 0.82	2.41 ± 0.97	296 ± 118	15.33 ± 4.69	15.39 ± 3.54
V1.3	2	15.43 ± 0.27	15.5 ± 0.25	23.20 ± 0.55	20.83 ± 0.82	2.37 ± 0.99	301 ± 123	15.02 ± 4.76	15.07 ± 3.58
20 September 2001, IMF on calcite = −7.83 ± 0.65 ‰, IMF on quartz = −11.5 ± 0.46 ‰[d]									
Brazil Qz (9.60 ‰)	Std Qz	−1.61 ± 0.24		9.89 ± 0.52					
Brazil Qz	Std Qz	−2.30 ± 0.32		9.20 ± 0.56					
Brazil Qz	Std Qz	−2.01 ± 0.23		9.49 ± 0.51					
Brazil Qz	Std Qz	−1.85 ± 0.29		9.65 ± 0.54					
Brazil Qz	Std Qz	−1.19 ± 0.25		10.31 ± 0.52					
Brazil Qz	Std Qz	−2.44 ± 0.21		9.06 ± 0.50					
Mex (23.64 ‰)	Std Cc		15.20 ± 0.30		23.03 ± 0.72				
Mex	Std Cc		16.52 ± 0.28		24.35 ± 0.71				
Mex	Std Cc		15.89 ± 0.31		23.72 ± 0.72				
Mex	Std Cc		16.35 ± 0.31		24.18 ± 0.72				
Mex	Std Cc		15.09 ± 0.29		22.92 ± 0.71				
V2b.3 at 8 m	3	8.91 ± 0.24	7.82 ± 0.29	20.41 ± 0.52	15.65 ± 0.71	4.76 ± 0.88	132 ± 43	1.04 ± 4.71	0.98 ± 4.02
V2b.3	3	9.89 ± 0.20	8.42 ± 0.28	21.39 ± 0.5	16.25 ± 0.71	5.14 ± 0.87	116 ± 38	0.24 ± 4.75	0.08 ± 4.10
V2b.3	4	10.21 ± 0.18	8.91 ± 0.31	21.71 ± 0.49	16.74 ± 0.72	4.97 ± 0.87	123 ± 40	1.35 ± 4.72	1.24 ± 4.06
V2b.3	4	9.68 ± 0.30	9.86 ± 0.23	21.18 ± 0.55	17.69 ± 0.69	3.49 ± 0.88	200 ± 64	7.75 ± 4.46	7.89 ± 3.62
V2b.3	4	8.74 ± 0.33	9.79 ± 0.24	20.24 ± 0.57	17.62 ± 0.69	2.62 ± 0.89	272 ± 97	10.88 ± 4.37	10.98 ± 3.35
V2b.9 at 200 m	3	7.18 ± 0.36	9.49 ± 0.23	18.68 ± 0.58	17.32 ± 0.69	1.36 ± 0.90	484 ± 254	15.22 ± 4.27	14.77 ± 2.71
V2b.9	4	9.93 ± 0.23	11.34 ± 0.21	21.43 ± 0.51	19.17 ± 0.68	2.26 ± 0.85	314 ± 115	13.75 ± 4.12	13.77 ± 3.06
V2b.4 at 12 m	3	11.23 ± 0.20		22.73 ± 0.50					
V2b.4	3	10.65 ± 0.29		22.15 ± 0.54					
V2b.4	4	12.86 ± 0.23	12.64 ± 0.25	24.36 ± 0.51	20.47 ± 0.7	3.89 ± 0.87	175 ± 55	9.06 ± 4.46	9.17 ± 3.69
V2b.4	4	12.01 ± 0.29	13.09 ± 0.25	23.51 ± 0.54	20.92 ± 0.7	2.59 ± 0.88	276 ± 98	14.29 ± 4.32	14.39 ± 3.31
21 September 2001, IMF on calcite = −6.03 ± 0.59 ‰, IMF on quartz = −7.75 ± 0.32 ‰[d]									
Brazil Qz (9.60 ‰)	Std Qz	1.85 ± 0.17		9.60 ± 0.36					
Brazil Qz	Std Qz	1.47 ± 0.28		9.22 ± 0.42					
Brazil Qz	Std Qz	2.25 ± 0.33		10.00 ± 0.46					
Brazil Qz	Std Qz	1.84 ± 0.23		9.59 ± 0.39					
Mex (23.64 ‰)	Std Cc		17.97 ± 0.20		24.00 ± 0.62				
Mex	Std Cc		17.24 ± 0.26		23.27 ± 0.64				
Mex	Std Cc		17.89 ± 0.26		23.92 ± 0.64				
Mex	Std Cc		16.77 ± 0.18		22.80 ± 0.61				
Mex	Std Cc		18.18 ± 0.20		24.21 ± 0.62				
V2b.1 at 1 m	3	10.59 ± 0.30	12.63 ± 0.18	18.34 ± 0.44	18.66 ± 0.61	−0.32 ± 0.77	...	...	...
V2b.1	3	9.87 ± 0.27	13.14 ± 0.14	17.62 ± 0.42	19.17 ± 0.60	−1.55 ± 0.95	...	...	...
V2b.2 at 3 m	3	11.75 ± 0.20	13.98 ± 0.22	19.50 ± 0.39	20.01 ± 0.63	−0.51 ± 0.74	...	...	...
V2b.2	3	10.64 ± 0.29	14.14 ± 0.24	18.39 ± 0.44	20.17 ± 0.64	−1.78 ± 0.78	...	...	...
V2b.2	4	12.27 ± 0.31	15.79 ± 0.21	20.02 ± 0.45	21.82 ± 0.63	−1.80 ± 0.77	...	...	...
V2b.2	4	11.99 ± 0.29	14.74 ± 0.28	19.74 ± 0.44	20.77 ± 0.65	−1.03 ± 0.78	...	...	...
21 September 2001 (Continued) After Beam Refocused, IMF on calcite = −7.80 ± 0.39 ‰, IMF on quartz = −10.82 ± 0.48 ‰[d]									
Brazil Qz (9.60 ‰)	Std Qz	−0.61 ± 0.22		10.21 ± 0.52					
Brazil Qz	Std Qz	−1.30 ± 0.27		9.52 ± 0.55					
Brazil Qz	Std Qz	−1.76 ± 0.28		9.06 ± 0.55					
Brazil Qz	Std Qz	−1.11 ± 0.24		9.71 ± 0.53					
Brazil Qz	Std Qz	−1.31 ± 0.15		9.51 ± 0.50					
Mex (23.64 ‰)	Std Cc		15.67 ± 0.22		23.47 ± 0.45				
Mex	Std Cc		16.34 ± 0.17		24.14 ± 0.43				
Mex	Std Cc		15.92 ± 0.18		23.72 ± 0.43				
Mex	Std Cc		15.42 ± 0.93		23.22 ± 0.41				
V2b.8 at 80 m	3	10.80 ± 0.41	12.32 ± 0.16	21.62 ± 0.63	20.12 ± 0.61	1.50 ± 0.88	448 ± 214	17.50 ± 4.17	17.16 ± 2.73
V2b.8	3	10.95 ± 0.30	11.20 ± 0.29	21.77 ± 0.56	19.00 ± 0.65	2.77 ± 0.86	257 ± 87	11.71 ± 4.23	11.83 ± 3.28
V2b.8	4	11.71 ± 0.22	12.54 ± 0.28	22.53 ± 0.52	20.34 ± 0.65	2.19 ± 0.83	324 ± 117	15.18 ± 4.03	15.18 ± 2.97
V2b.8	4	11.61 ± 0.33	12.15 ± 0.23	22.43 ± 0.58	19.95 ± 0.63	2.48 ± 0.86	288 ± 101	13.72 ± 4.18	13.80 ± 3.16
V2b.7 at 60 m	3	14.10 ± 0.23	14.38 ± 0.20	24.92 ± 0.53	22.18 ± 0.44	2.74 ± 0.69	261 ± 73	15.02 ± 3.48	15.14 ± 2.67
V2b.7	3	13.35 ± 0.21	13.70 ± 0.21	24.17 ± 0.52	21.50 ± 0.44	2.67 ± 0.68	268 ± 74	14.59 ± 3.43	14.70 ± 2.62
V2b.7	3	12.05 ± 0.23	11.45 ± 0.21	22.87 ± 0.53	19.25 ± 0.62	3.62 ± 0.82	191 ± 57	8.83 ± 4.19	8.97 ± 3.42
V2b.5 at 20 m	3	12.39 ± 0.29	12.08 ± 0.15	23.21 ± 0.56	19.88 ± 0.61	3.33 ± 0.83	211 ± 65	10.53 ± 4.19	10.68 ± 3.37
V2b.5	4	11.69 ± 0.26	11.72 ± 0.26	22.51 ± 0.54	19.52 ± 0.62	2.99 ± 0.82	238 ± 75	11.42 ± 4.11	11.56 ± 3.23
V2b.5	4	11.77 ± 0.33	12.18 ± 0.19	22.59 ± 0.53	19.98 ± 0.62	2.61 ± 0.82	274 ± 90	13.28 ± 4.02	13.38 ± 3.07

Table 2. (continued)

Sample	$Q_z - C_c$ Pair	$^{18}O/^{16}O$ Q_z ± 1σ, ‰	$^{18}O/^{16}O$ C_c ± 1σ, ‰	$\delta^{18}O_{Qz/SMOW}$ ± 1σ, ‰	$\delta^{18}O_{Cc/SMOW}$ ± 1σ, ‰	Δ_{Qz-Cc}, ‰	T,[a] °C	$\delta^{18}O_{H2O}$, ‰ $(Q_z - H_2O)$[b]	$\delta^{18}O_{H2O}$, ‰ $(C_c - H_2O)$[c]
V2b.6 at 45 m	3	12.85 ± 0.32	12.86 ± 0.26	23.67 ± 0.58	20.66 ± 0.47	3.01 ± 0.75	236 ± 68	12.50 ± 3.78	12.65 ± 2.96
V2b.6	4	15.10 ± 0.26	14.80 ± 0.17	25.92 ± 0.55	22.60 ± 0.43	3.32 ± 0.70	212 ± 57	13.30 ± 3.63	13.45 ± 2.90
V2b.6	4	13.40 ± 0.23	14.19 ± 0.25	24.22 ± 0.53	21.99 ± 0.46	2.23 ± 0.70	319 ± 98	16.70 ± 3.45	16.71 ± 2.53

[a]Temperature calculated from the fractionation between quartz and calcite using the calibration of *Sharp and Kirschner* [1994]. The 1σ error calculation is detailed in Appendix A.

[b]O isotope composition of water in equilibrium with quartz at T°, calculated using the calibration of *Sharp and Kirschner* [1994]. The 1σ error calculation is detailed in Appendix A.

[c]O isotope composition of water in equilibrium with calcite at T°, calculated using the calibration of *Zheng* [1999]. The 1σ error calculation detailed in Appendix A.

[d]Instrumental mass fractionation is calculated from the averaged results of replicate spot−to-spot measurements on standards. The ±1σ SD on the average is the external reproducibility on standards.

Graham et al., 1996; *Rollion-Bard et al.*, 2003]. No instrumental drift exceeding the external reproducibility on standards was detected. The IMFs in quartz and calcite were therefore corrected using the average IMF values based on standard measurements (Table 2). These corrections and their accuracy are comparable to those of other quartz and calcite O isotope studies using the Cameca IMS 1270 of the CRPG [*Aléon et al.*, 2002; *Rollion-Bard et al.*, 2003]. A systematic difference of 2.7 ± 1 ‰ was observed between quartz and calcite IMFs, quartz being more fractionated. The total 1σ uncertainty of O isotope analyses was considered as the sum of (1) the precision of a single O isotope measurement, limited by the internal error due to counting statistics, and (2) the accuracy on the determination of the IMFs, limited by the external reproducibility on standards.

[20] The probed areas were checked after analysis by optic microscopy in order to eliminate any data coming from spots biting on the quartz-calcite contact. Differences in fractionation between quartz and calcite ($\Delta_{Qz-Cc} = \delta^{18}O_{Qz} - \delta^{18}O_{Cc}$) were converted into temperatures using the calibration of *Sharp and Kirschner* [1994], based on natural isotopic variations (including Tinos Marble). Quartz-water and calcite-water fractionations were calculated using the equations of *Sharp and Kirschner* [1994] and *Zheng* [1999], respectively. The calculation of the 1σ error on the determination of temperatures and water O isotopes ratios is detailed in appendix.

5. Results

5.1. Cathodoluminescence Imaging

[21] On the basis of optical observations and CL imaging, two end-member generations of quartz and calcite were recognized in V1. Generation 1 consists of lenticular-shaped coarse grains displaying undulose extinction (quartz and calcite) and intersected twins (calcite, Figure 7a) that are surrounded with dynamically recrystallized domains lining the foliation plane. Quartz 1 is nonluminescent in CL, whereas calcite 1 is dark red and surrounded with bright yellow reequilibration rims (Figures 7b and 7d). Quartz-calcite 1 are the oldest relics preserved in V1, and thus can be considered as synchronous to this veining event, formed in ductile context before or during the blueschist to greenschist facies decompression path. Quartz-calcite 2 occurs in shear bands cutting across the lens-shaped relics of quartz-calcite 1 (Figures 7c and 7d). Dark violet luminescent quartz 2 occurs as anhedral grains lining the bright yellow/orange calcite 2 that rims calcite 1 (Figure 7d). Quartz-calcite 2 occurs locally in association with chlorite flakes and was likely equilibrated during a (late?) increment of ductile deformation attending greenschist facies metamorphism. Consequently, this generation of quartz and calcite is attributed to the V2a vein stage.

[22] Two main generations of quartz and calcite presenting an equilibrium texture were also recognized in V2b veins. Quartz-calcite 3, which represents the main filling assemblage of V2b, occurs as euhedral crystals with sharp, well defined grain boundaries (Figure 7e). Quartz 3 is limpid and not luminescent in CL, whereas calcite 3 displays a homogeneous reddish luminescence (Figure 7f). Quartz-calcite 3 is considered to be cogenetic to the V2b stage and thus to the late ductile-early brittle deformation event experienced by this vein type. Quartz-calcite 4 occurs as millimeter-scale grains filling fractures and associated voids that cut across quartz-calcite 3 (Figures 7g and 7h). The fracture planes are oriented parallel to fluid inclusion trails and define bright orange bands in CL (Figure 7h). The formation of quartz-calcite 4 may be associated with the reopening of folded joints and en echelon veins by late N-S

Figure 7. Microstructures and $\delta^{18}O$ mapping in V1 and V2b veins, on the example of samples V1.1 and V2b.3, taken at 8 m under the detachment (images location in Figures 3b and 3f). (a) Optic imaging of generation 1 quartz and calcite in V1 vein (sample V1.1). (b) Cathodoluminescence (CL) imaging of Figure 7a, with corresponding temperatures around 350°C using $\delta^{18}O$ fractionation between quartz and calcite. (c) Optic imaging of generation 2 in V1 at 8 m under the contact (sample V1.1). (d) CL imaging of Figure 7c, with temperatures around 225°C. (e) Optic imaging of generation 3 quartz and calcite in V2b vein sampled at 8 m under the detachment (sample V2b.3). (f) CL imaging of Figure 7e, with temperature around 120°C. (g) Optic imaging of generation 4 in V2b at 8 m under the contact (sample V2b.3). (h) CL imaging of Figure 7g with $\delta^{18}O$ temperatures between 120° and 270°C. See color version of this figure at back of this issue.

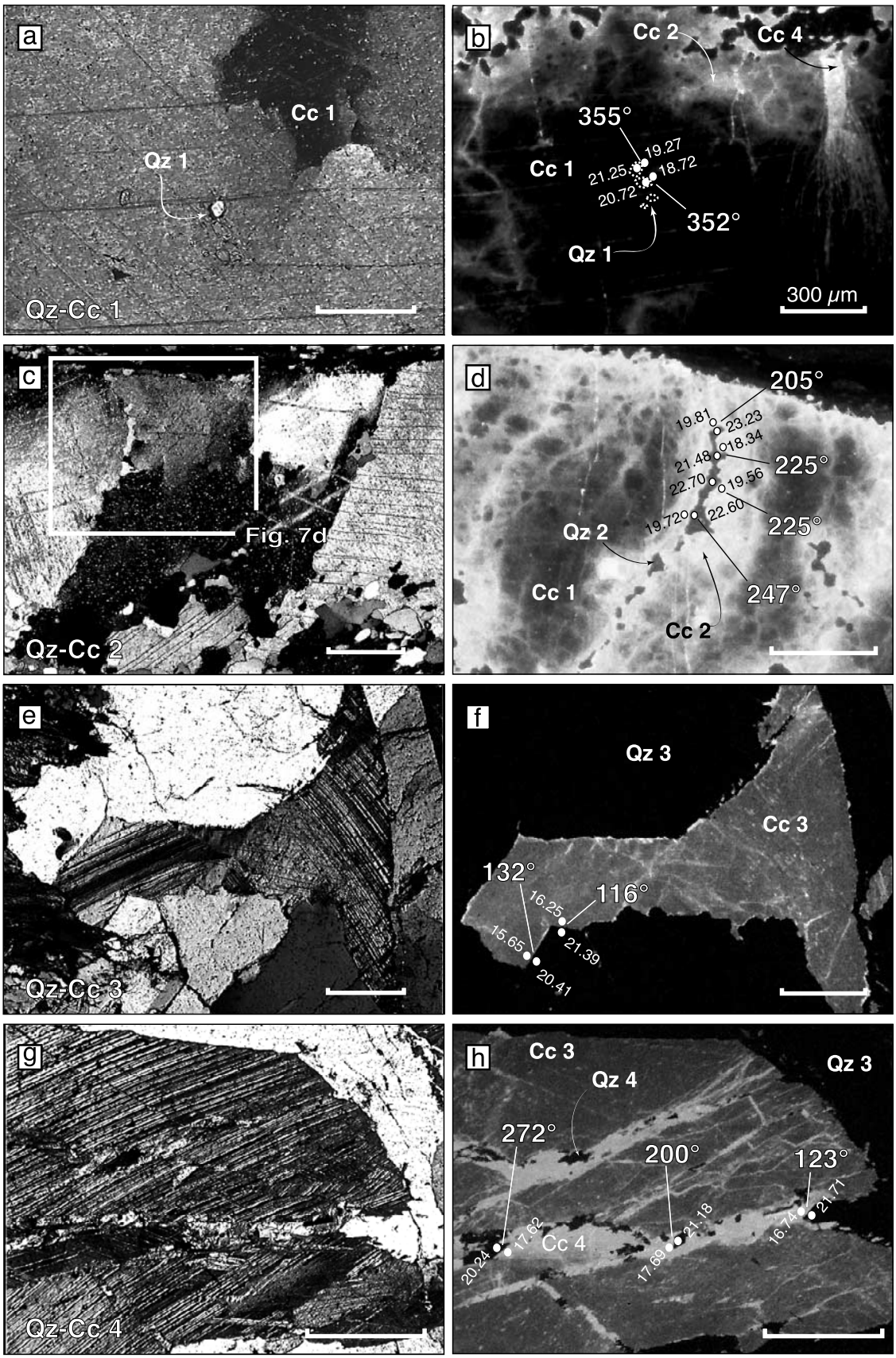
a
Cc 1
Qz 1
Qz-Cc 1
b
Cc 2
Cc 4
355°
19.27
Cc 1
21.25
18.72
20.72
352°
Qz 1
300 μm
c
Fig. 7d
Qz-Cc 2
d
205°
19.81
23.23
18.34
21.48
225°
22.70
19.56
19.72
22.60
225°
Qz 2
Cc 1
247°
Cc 2
e
Qz-Cc 3
f
Qz 3
Cc 3
132°
16.25
116°
15.65
21.39
20.41
g
Qz-Cc 4
h
Cc 3
Qz 4
Qz 3
272°
200°
123°
21.71
16.74
17.62
20.24
Cc 4
21.18
17.69

Figure 7

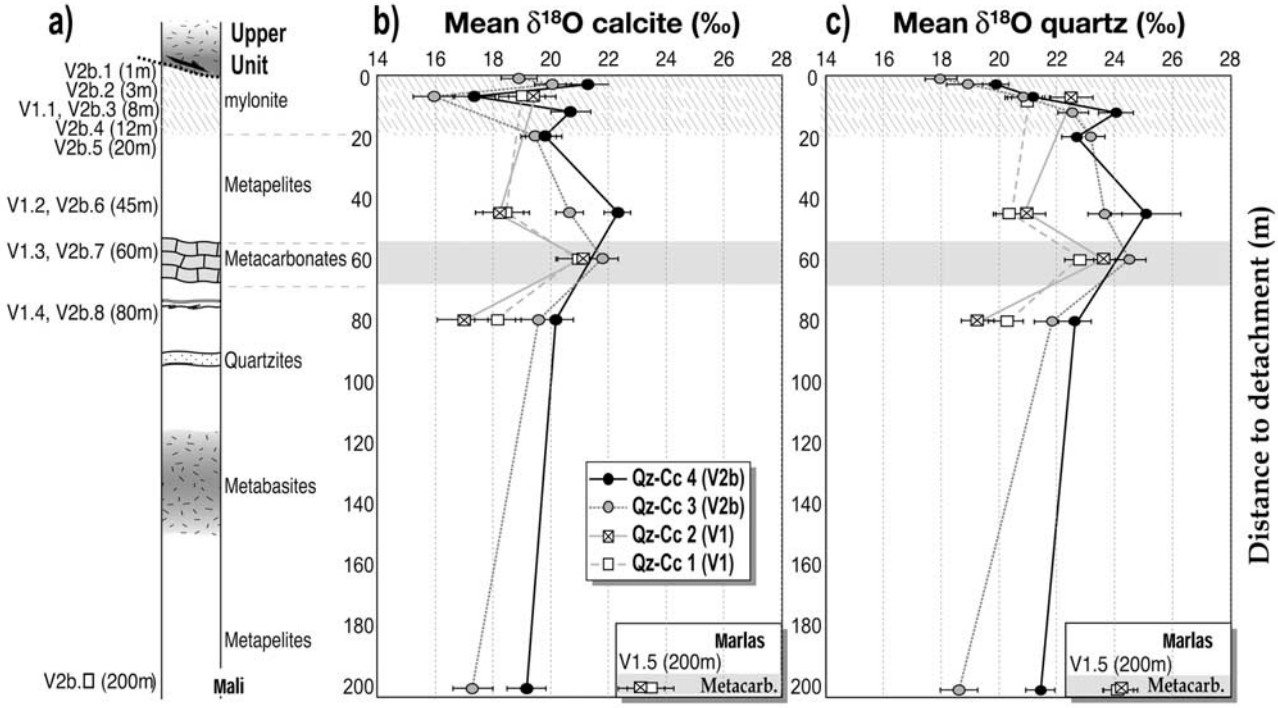

Figure 8. Quartz and calcite $\delta^{18}O$ values as a function of distance to detachment and lithology. (a) Simplified log of Mali, with structural position of samples under the detachment. (b and c) Mean of ion microprobe $\delta^{18}O$ measurements in veins as a function of distance to detachment along the traverse of Mali, with host rock lithologies. "Reference" sample from Marlas (sample V1.5) also reported. Open squares show the values for generation 1 quartz and calcite in V1 veins. Crossed squares show generation 2 in V1. Shaded circles show generation 3 in V2b. Solid circles show generation 4 in V2b. Quartz data given in Figure 8b and calcite data given in Figure 8c.

V2b. Yet, it cannot be excluded that part of the fracturation formed during the V3 stage.

[23] As each quartz-calcite generation is identified by a same CL texture in all the samples, the V1 + V2b system is considered below to preserve four crystallization/deformation events that initiated along the decompression path during blueschist to greenschist facies metamorphism in the ductile regime, and ended in the brittle field in shallow crustal levels.

5.2. Oxygen Isotope Composition and Temperature Estimates

[24] Ion microprobe $\delta^{18}O$ measurements on quartz and calcite and calculated fractionation factors, temperatures and isotopic composition of equilibrium waters are given in Table 2. Figure 8 shows the mean $\delta^{18}O$ values of the different quartz-calcite pairs as a function of the distance to the detachment and vein host rock lithology at Mali. Also shown are the $\delta^{18}O$ values of quartz-calcite 1 and 2 from the blueschist facies metacarbonate at Marlas. The $\delta^{18}O$ of calcite 1 ranges between 21 to 23 ‰ in metacarbonates, and 18 to 19 ‰ in metapelites and mylonites (Figure 8b). The $\delta^{18}O$ of quartz 1 is $\sim$ 23–24 ‰ in metacarbonates, and around 20–21 ‰ in metapelites and mylonitic rocks of the contact (Figure 8c). These data fall in the range of isotopic composition for medium-grade marine metasediments. For quartz and calcite, the general tendency is to increase fractionation as the generation is younger. With regard to pairs 2, 3 and 4, a consequence of this fractionation increase is the gradual disappearance of isotopic differences between the metacarbonate layer and the surrounding metapelites. In the mylonite zone, note that quartz 3 and 4 show a marked depletion in ^{18}O within 20 m toward the contact, whereas the ^{18}O content of calcite 3 and 4 is highly variable.

[25] Figures 9a, 9b, 9c, and 9d plot calculated temperatures for the four pairs of quartz-calcite pairs as a function of the distance to the detachment. An example of temperature calculation from $\delta^{18}O$ mapping is shown in Figure 7 (complete $\delta^{18}O$ and temperature mapping for all the samples studied is available in auxiliary material[1]). Δ_{Qz-Cc} of quartz-calcite 1 from 200 m to 8 m beneath the detachment range between 1.7 and 2 ‰, yielding temperatures of $\sim$ 350°–400°C ± 150°C (Figure 9a). Δ_{Qz-Cc} of quartz-calcite 2 shifts from 1.7 to 3.4 ‰ between 200 m and 8 m under the detachment. Corresponding calculated temperatures range between 400 and 200°C (Figure 9b). The fractionation between quartz and calcite in generation 3 (V2b) decreases from about 1.3 ‰ at 200 m (sample V2b.9) to 5 ‰ at 8 m (sample V2b.3) under the fault surface. This

[1] Auxiliary material is available at ftp://ftp.agu.org/apend/tc/2003TC001509.

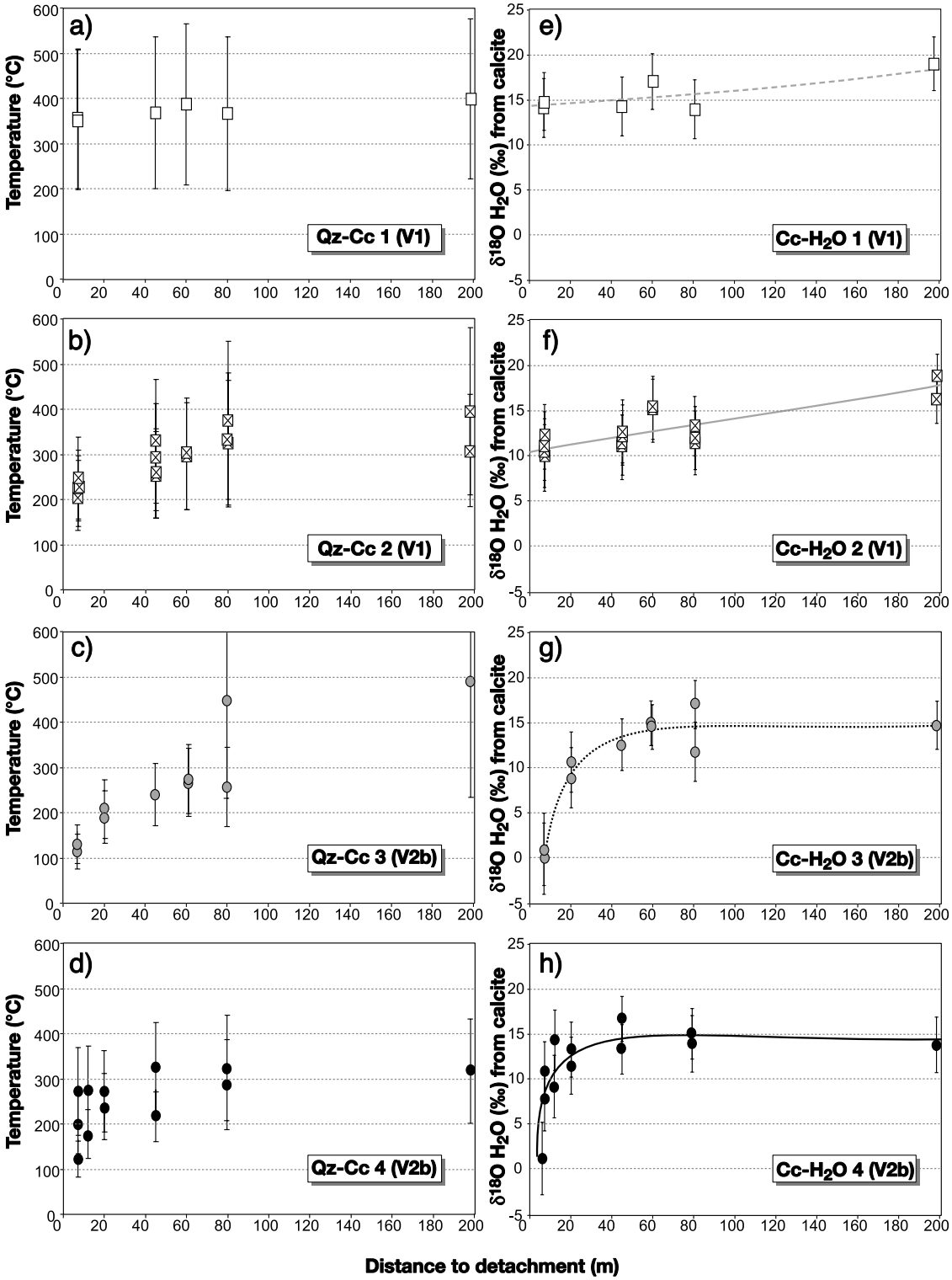
a)
Qz-Cc 1 (V1)
e)
Cc-H2O 1 (V1)
b)
Qz-Cc 2 (V1)
f)
Cc-H2O 2 (V1)
c)
Qz-Cc 3 (V2b)
g)
Cc-H2O 3 (V2b)
d)
Qz-Cc 4 (V2b)
h)
Cc-H2O 4 (V2b)
Temperature (°C)
δ18O H2O (‰) from calcite
Distance to detachment (m)

Figure 9

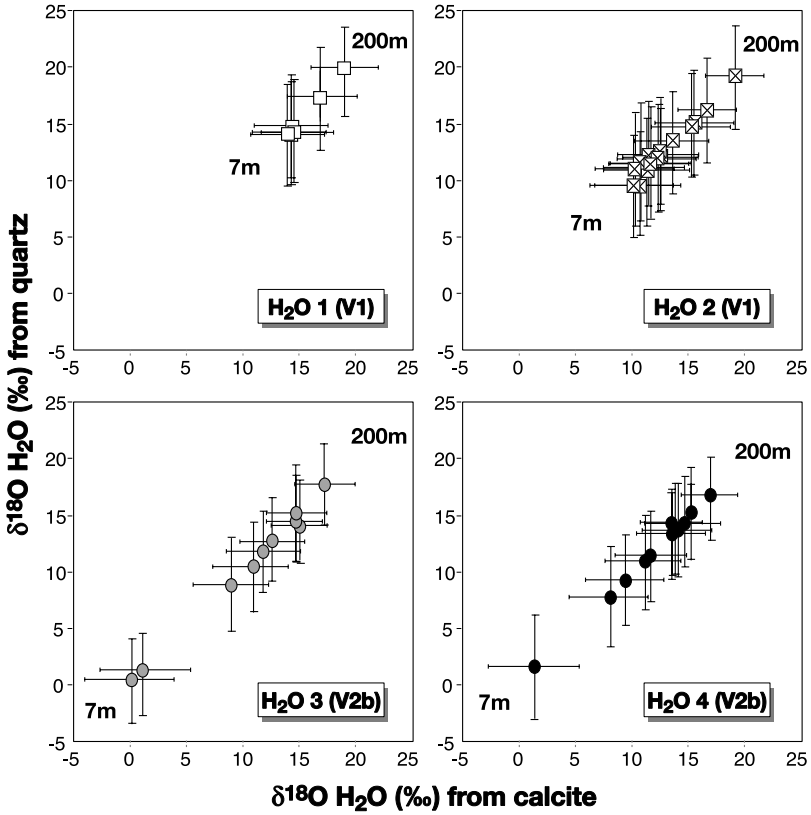

Figure 10. The $\delta^{18}O$ of water calculated from quartz (using the calibration of *Sharp and Kirschner* [1994]) versus $\delta^{18}O$ of water calculated from calcite (using the calibration of *Zheng* [1999]) at the temperatures of generations 1, 2, 3, 4 (see Figures 8a–8d). Distance to detachment is also reported. Similar values are obtained by using any of the two calibrations.

shift corresponds to a minimum temperature decrease of 100°C in 192 m along the traverse. Δ_{Qz-Cc} of quartz-calcite 4 display variations from 2.2 ‰ at 200 m to 2.6–3.9 ‰ at 8 m beneath the contact. Despite a wide dispersion, temperature at 200 m (320° ± 120°C; sample V2b.9) is at least 30°C higher than the minimum value at 8 m (127° ± 41°C; sample V2b.3, Figure 9d). Low and even negative isotopic fractionation factors are observed in some quartz-calcite pairs from samples V1.5 (200 m), V2b.2 (3 m) and V2b.1 (1 m). This indicates that quartz and calcite from these pairs are not in isotopic equilibrium, despite their apparent equilibrium texture (see below).

[26] Knowing the temperature of mineral equilibration, it is possible to calculate the $\delta^{18}O$ of water in equilibrium with the four generations of calcite (Figures 9e, 9f, 9g, and 9h) and quartz (Figure 10). The $\delta^{18}O_{H2O}$ calculated using calcite 1 clusters between 20 ‰ and 15 ‰ (Figure 9e). These values are in the range of metamorphic aqueous fluids [*Sheppard*, 1986]. The $\delta^{18}O_{H2O}$ in equilibrium with calcite 2 decreases from 18 ± 3 ‰ at 200 m (sample V1.5) to 11 ± 3 ‰ (sample V1.1) at 8 m under the detachment (Figure 9f). The decrease is quasilinear throughout the considered section. The $\delta^{18}O_{H2O}$ inferred from calcite 3 decreases from 15 ± 4 ‰ at 200 m (sample V2b.9) to 0 ± 4 ‰ (sample V2b.3) at 8 m under the contact (Figure 9g). This ~15 ‰ decrease is restricted to 50 m (sample V2b.6) below the detachment. The $\delta^{18}O_{H2O}$ calculated using calcite 4 decreases from 15 ± 4 ‰ at 200 m (sample V2b.9) to 1.3 ± 4 ‰ at 8 m (sample V2b.3, Figure 9h). This ~13 ‰ decrease is mainly restricted within 20 m beneath the detachment. Similar isotopic shifts are obtained using the quartz-water fractionation calibration from *Sharp and Kirschner* [1994] at the same temperatures (Figure 10).

6. Discussion

6.1. Isotopic Equilibrium

[27] In order to interpret $\delta^{18}O$ data in terms of temperatures, it is important to assess whether quartz and calcite

Figure 9. (a–d) Temperatures calculated from quartz-calcite fractionation and (e–h) O isotopes ratios of water in equilibrium with calcite, as a function of distance to detachment (Q_z-C_c and C_c-H_2O calibrations from *Sharp and Kirschner* [1994] and *Zheng* [1999], respectively). Generation 1 quartz-calcite pairs in V1 veins (Figures 9a and 9e). Generation 2 in V1 (Figures 9b and 9f). Generation 3 in V2b (Figures 9c and 9g). Generation 4 in V2b (Figures 9d and 9h).

equilibrated microtextures reflect isotopic equilibrium. Isotopic equilibria yielding geologically relevant isotopic temperatures are obtained if (1) both quartz and calcite were coprecipitated from a same fluid and were not later affected by diffusion, (2) one of the minerals precipitated after the other, and a rim of complete reequilibration with the new fluid developed on the preexisting mineral, or (3) a rim of reequilibration developed on two preexisting minerals by diffusional exchange with the new fluid.

[28] Isotopic equilibrium (1) should be preserved in quartz-calcite pairs unaffected by ductile deformation and displaying sharp contacts (e.g., quartz-calcite 3 and 4, Figure 7f, h), and in quartz-calcite assemblages protected within the core of large grain relics (quartz-calcite 1, Figure 7b). Isotopic reequilibration (2) and (3) should be found in deformed zones such as shear bands cutting across quartz and calcite relics. However, because the rims of quartz are undercontrasted compared to the bright yellow rims of calcite grains, it is difficult to control the texture of quartz by CL. Situations (2) and (3) involving quartz reequilibration should therefore not be used as equilibrium pairs. This precaution avoids temperature errors arising from a more sluggish O isotope diffusion in quartz than in calcite. In contrast, considering that oxygen diffusion in calcite is faster than the diffusion of any of the CL exciting elements (divalent cations) [*Fisler and Cygan*, 1999], the oxygen isotope equilibration rim in calcite should be equal or wider than the observed CL rim. Situation (2) with quartz as the neoprecipitated mineral and calcite as the reequilibrated mineral can be therefore considered safe to use as an equilibrium pair (e.g., quartz-calcite 2, Figure 7d).

[29] In the following discussion we will thus assume that isotopic equilibrium is achieved along grain contacts within a ~20-μm-large band, which corresponds to the size of the area probed by the Cs^+ beam. In the case where equilibrium was disturbed by solid-state diffusion after the frozen-in texture, the error on temperature estimation is predictable. As shown by *Farver* [1990] and *Farver and Yund* [1991], oxygen diffusion activation energy is lower in calcite than in quartz. Any late reopening of the quartz-calcite thermometer, by deformation, temperature or fluid activity should thus mostly affect calcite. Taking into account the general increase in ^{18}O content as calcite generation is younger (Figure 8b), the effect of a reopening of the thermometer would be to rise the $\delta^{18}O$ of calcite toward the value of quartz, and thus to unduly lower the quartz-calcite fractionation with respect to the equilibrium value. This would lead to overestimated temperatures and O isotopic ratios of water, especially in the most easily reopened region, e.g., closer to the detachment. This effect could explain the low and even negative quartz-calcite fractionations in samples V2b.1, and V2b.2, immediately beneath the contact (Table 2). It should therefore be kept in mind that if isotopic disequilibrium occurred in the other samples, its effect would be to smooth the temperature variations compared to the real gradients, not to increase them. Furthermore, since the isotopic temperatures also matches the lower temperature limit given by homogenization data of fluid inclusions in the same veins [*Famin et al.*, 2004], the isotopic temperatures can reasonably be considered as geologically relevant.

6.2. Thermal Regime

[30] Ion microprobe determination of $\delta^{18}O$ provides estimates of the temperatures at which the four texturally equilibrated quartz-calcite pairs were formed in V1 and V2b veins. At any given distance to the detachment, the temperature recorded by the younger pair is equal or lower than the temperature of the former pair (e.g., Figures 7b, 7d, 7f, and 7h). This temperature decrease from a pair to the next is interpreted to reflect multiple stages of quartz-calcite equilibration, frozen in at different times of the deformation history. High temperature record was fossilized in less-deforming regions of the veins while the quartz-calcite thermometer was rejuvenated down to lower temperatures in deforming regions.

[31] Results also show that the temperature range between end-members quartz-calcite generations increases toward the fault. Temperatures of predetachment faulting were estimated by mineralogical assemblages and quartz-magnetite thermometry to be 440°–470°C in deeper portion of the metamorphic dome [*Bröcker et al.*, 1993; *Parra et al.*, 2002]. The oxygen isotope temperatures of quartz-calcite 1 pairs are in the same range, within uncertainties (Figure 9a). For later quartz-calcite 2, calculated temperatures are in the range 200°–400°C, the lowest values being reached beneath the detachment (Figure 9b). Temperatures recorded in quartz-calcite 3 show a major decrease of 145°C in about 50 m toward the fault (Figure 9c). Although more widespread, calculated temperatures using quartz-calcite 4 show a decrease of 190°C along the traverse. As for quartz-calcite 3, temperature shift is restricted in a ~20 m distance beneath the detachment. It is worth noting that the temperature fall recorded by O isotopes closely matches the decrease of homogenization temperatures of fluid inclusions in greenschist facies veins, from ~350°C to ~180°C toward the detachment [*Famin et al.*, 2004].

[32] There are three end-member explanations to the data.

[33] 1. At isothermal condition of ~200°C, the temperature shift reflects a complete isotopic equilibration beneath the fault where deformation is maximum, and a fading away of this reequilibration far under the detachment, as deformation intensity vanishes out. This interpretation, however, can be readily dismissed for textural as well as isotopic reasons. The fading away of deformation intensity would be observable both in vein shapes and in CL textures. Moreover, considering that calcite rejuvenation results in a $\delta^{18}O$ rise, the most efficiently reset quartz-calcite pairs would have recorded the lowest fractionations. As such, the highest temperatures should have been found near the detachment.

[34] 2. The data can also be interpreted to document the progressive cooling path of the footwall during exhumation, the younger quartz-calcite pairs (the cooler) occurring closer to the detachment. However, this interpretation is also unlikely, again for textural reasons. A ~140°C fall such as recorded by quartz-calcite pairs 3 and 4 would take about

6 Ma (for each pair) to occur by exhumation alone, considering the cooling rate of 20°C/Ma defined by *Parra et al.* [2002]. Given the uniform CL textures along the traverse, each vein set is likely quasisynchronous and the time span recorded by each quartz-calcite generation is certainly much shorter than 6 Ma, otherwise deformation pattern would be very different at the two ends of the transect. Besides, a 6 Ma time span for each quartz-calcite generation seems huge compared to the overall duration of the retrogression event. Conductive cooling by exhumation certainly occurred, but is unlikely to explain alone the shift observed.

[35] 3. Another possible interpretation is that spatial temperature gradients were present in the footwall during the time slots of the four quartz-calcite pairs isotopic equilibration. The above temperature gradients are one or two orders of magnitude greater than conductive spatial gradients typically produced by the juxtaposition of cold hanging wall rocks on a hotter footwall [*Bertotti and ter Voorde*, 1994], even considering the isotherms uplift enhanced by the bulge of the core complex [*Mancktelow and Grasemann*, 1997]. The only viable mechanism for heat transport on this scale is thus advection of fluids. We interpret the four thermal gradients to document progressive cooling (quartz-calcite 2, 3, 4) of the footwall from ambient predetachment temperatures (quartz-calcite 1) by means of advective heat extraction by fluid circulation. This conclusion agrees with that of *Morrison and Anderson* [1998], who interpreted a geotherm of 2160°C/km along the Whipple Mountain detachment as fluid advection-induced cooling. In addition to their pioneering work, this study provides constraints on the relative timing of fluid circulation along a crustal detachment with respect to the deformation history. Massive cooling was recorded mainly in late ductile to early brittle textures (quartz-calcite 3, 4).

6.3. Fluid Source

6.3.1. Fluids at V1 Stage

[36] Ion probe oxygen isotope measurements have been compared to data available in the literature. Figure 10 plots mean $\delta^{18}O$ values of quartz 1 and calcite 1 (this study), and bulk quartz-calcite fluorination analyses on V1 veins [*Famin et al.*, 2000] as a function to the distance of the detachment. The data are compared to mean wall rock quartz and calcite analyses from the SW part of Tinos [*Bröcker et al.*, 1993; *Ganor et al.*, 1996; *Matthews et al.*, 1999]. Following *Bröcker et al.* [1993] and *Ganor et al.* [1996], metabasites, metapelites, and marbles were plotted separately, but no distinction was made between blueschist and greenschist facies lithologies. Whole rock analyses [*Katzir et al.*, 1996] in metagabbros from the upper unit are also reported on a separate diagram in Figure 11.

[37] Using the data of *Bröcker et al.* [1993] and *Ganor et al.* [1996], wall rock $\delta^{18}O$ values at 800 m under the detachment are estimated at 16 and 17 ‰ for quartz in metabasites and metapelites, and 25 ‰ for calcite in marbles. As shown in Figure 11, V1-quartz 1 from metabasites and metapelites display a marked increase of 3 to 4 ‰ compared to wall rock values, whereas calcite 1 shows a decrease of ~5 ‰ compared to wall rock. Importantly, note that bulk fluorinated quartz (V1 in metabasites), quartz 1 (V1 in metapelites) and calcite 1 (V1 in marbles) $\delta^{18}O$ converge to similar values of 19–21 ‰ near the fault. Water in equilibrium with such isotopic signatures is close to 14–16 ‰, in the range of rock-buffered fluids. These variations are directly correlated to the distance of the detachment, and suggest an isotopic disequilibrium between V1 veins and their host rock. These variations result in a homogenization of $\delta^{18}O$ values of quartz in V1 veins toward the detachment, irrespective to wall rock composition. We interpret this homogenization as a progressive mixing of O isotopes compositions of rock-buffered fluids from different lithologies, as strain localization initiates in the deep root of the shear zone. The lower $\delta^{18}O$ values were raised, whereas the higher decreased. The homogenization indicates that some fluids, either local or exotic, were already present in the deep blueschist facies root of the shear zone during the Eocene.

[38] An isotopic shift is also found in the upper unit. Whole rock oxygen isotope data on metagabbros from *Katzir et al.* [1996], reported as a function of distance to detachment on the left-hand side of Figure 11, show a ~6 ‰ ^{18}O enrichment of rocks in 60–80 m toward the contact. Although whole rock data can only be qualitatively compared with separated mineral values, the results clearly show a channel of O isotopes reequilibration around the fault.

6.3.2. Fluid Evolution

[39] The ^{18}O enrichment from wall rock to quartz 1 in V1 veins is also observed in veins from the older quartz-calcite pairs to the youngest (Figures 8b and 8c). This enrichment yields a decrease of the calculated $\delta^{18}O$ water composition as the quartz-calcite generation is younger (Figures 9e, 9f, 9g, and 9h), because the temperature drop (Figures 9a, 9b, 9c, and 9d) raises the fractionation between quartz or calcite and water. At 8 m under the detachment, the calculated $\delta^{18}O$ of water in equilibrium with calcite falls consistently from 15 ‰ in generation 1 (V1 veins) to 0 ‰ in generation 3 and 4 (V2b veins). This fall is mainly coeval with the opening of V2b veins and precipitation of quartz-calcite 3 and 4, but is already visible is quartz-calcite 2. As magmatic fluid should have $\delta^{18}O$ values of ~6 to 10 ‰, the fluids from which veins have formed are unlikely to be of igneous origin. Instead, the low and even negative $\delta^{18}O$ are best explained as surface-derived waters, marine or meteoric. Similar conclusions are drawn by taking quartz-water equilibria instead of calcite-water equilibria (Table 1 and Figure 10). Thus calculated $\delta^{18}O$ values are consistent with the arrival of surfaced-derived fluids that are cold relative to footwall rocks. The organic $\delta^{13}C$ signature of "postmetamorphic veins" documented by *Ganor et al.* [1994] on Tinos corroborates the interpretation of a superficial fluid source at the V3 stage. In the SW part of Tinos antiform, *Bröcker et al.* [1993] and *Ganor et al.* [1996] observed no $\delta^{18}O$ variations from blueschist facies lithologies and to greenschist facies ones other than lithological heterogeneities. They concluded that water/rock ratios were very low and that only small amounts of fluids had been involved in the retrogression. In contrast to *Bröcker et al.* [1993] and *Ganor et al.* [1996], we observe $\delta^{18}O$ variations from preserved

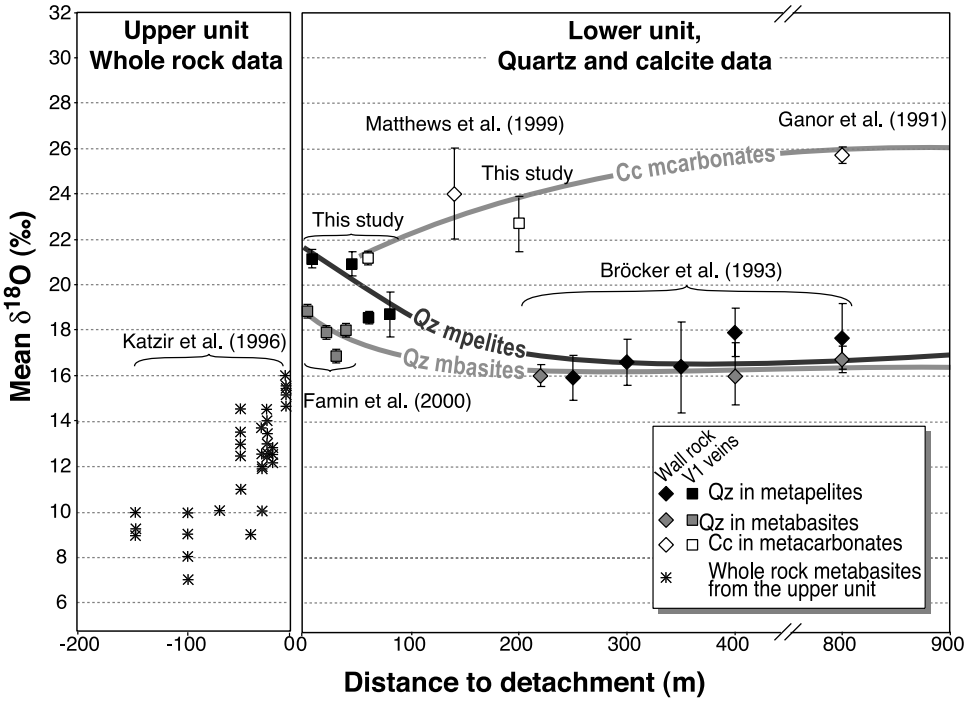

Figure 11. Synthetic plot showing quartz 1 and calcite 1 mean $\delta^{18}O$ in V1 veins (squares) reported together with literature wall rock quartz and calcite data in the lower unit of Tinos (diamonds), as a function of distance to detachment. Data from mineral separation and fluorination [*Bröcker et al.*, 1993; *Famin et al.*, 2000; *Ganor et al.*, 1991, 1996; *Matthews et al.*, 1999], and ion microprobe (this study). Open symbols indicate calcite 1 from V1 veins and from wall rock in metacarbonates. Shaded symbols indicate quartz 1 (V1) and from wall rock in metabasites. Solid symbols indicate quartz 1 (V1) and from wall rock in metapelites. Whole rock $\delta^{18}O$ data (stars) from variously deformed metagabbros of the upper unit [*Katzir et al.*, 1996] are also reported for qualitative comparison.

rocks on the SW to metamorphic veins on the NE, directly correlated to the vicinity of the detachment and independently of wall rock heterogeneities. The whole data set shows a progressive opening of the exhuming shear zone, from a rock-buffered closed system at the V1 stage to a water-buffered open system with the formation of V2b veins. Although a deep fluid source cannot be completely ruled out for quartz-calcite 1, the continuous oxygen isotope evolution of veins strongly suggests that meteoric fluids entered the ductile regime, at least during the formation of V2a, and possibly as deep as V1 veins.

6.4. Mechanisms of Fluid Circulation

[40] Figure 12 synthesizes the main interpretations deduced from structural and stable isotope data: (1) Small amounts of rock-buffered fluids were already present in the deep root of the ductile shear zone, down to blueschist facies depth (as suggested by the homogenized quartz 1 and calcite 1 isotopic values in V1 compared to wall rock $\delta^{18}O$, Figure 11). At this stage, the distribution of fluids (and shearing) was diffuse and spread out over a zone of at least 200 m beneath the shear zone. (2) Infiltration of surface-derived fluids increased during the early detachment stage veining with the greenschist-facies retrogression of the core complex (reworking of V1 veins by quartz-calcite 2, attributed to the V2a stage). Fluid supply exceeded the amount required for retrogression reactions to occur (as shown by the lowering of $\delta^{18}O$ values toward the contact), but was insufficient to disturb the conductive thermal regime of the footwall. This process may have been induced or enhanced by the progressive localization of the infiltration conduit, as V2a opening concentrated toward the detachment (Figure 5). (3) Infiltration drastically increased with the opening of V2b veins (quartz-calcite 3) in the late ductile-early brittle deformation stages, sufficiently to disturb the conductive thermal regime of the shear zone and the stable isotope signature of the impregnating fluids. This drastic inflow at the time of quartz-calcite 3 can be explained by structural data: No connected pathway existed as long as only N135°E trending V2b opened. The formation of the orthogonal N80°–N100°E set of veins in the vicinity of the contact (Figure 4) can have acted as a percolation threshold by connecting the vein network, and thus increasing permeability of two or three orders of magnitude. This effect may have been further enhanced by V2b vein concentration increase in the vicinity of the detachment (Figures 5 and 6). In this case, fluid flux was high enough and/or channelized enough to induce advective heat extraction and to prevent any ^{18}O interaction with wall rocks. Circulation was maximum inside of a 20- to 50-m conduit below the fault (quartz-calcite 3, 4, Figures 9g and 9h).

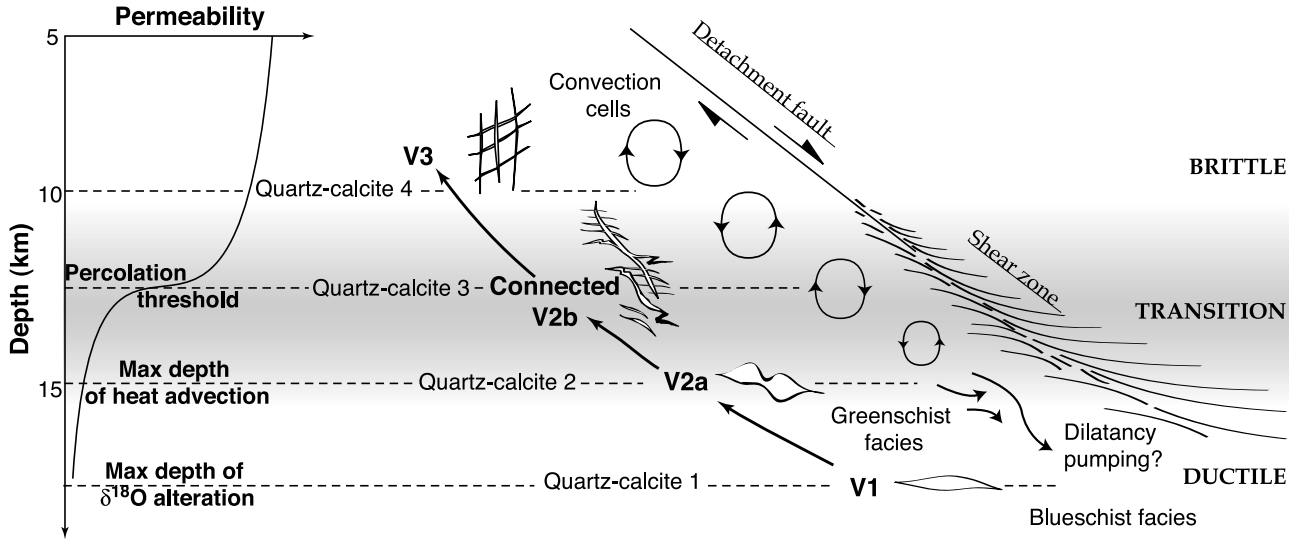

Figure 12. Synthetic diagram showing the simultaneous evolutions of veining, quartz-calcite precipitation, fracture permeability and fluid movement as the footwall of the shear zone enters the brittle regime during exhumation (not to scale). The appearance of an interconnected V2b vein network in late the ductile deformation context is interpreted as the mechanism responsible for fluid circulation increase (''percolation threshold'') recorded by oxygen isotopes in quartz-calcite 3.

[41] The most likely driving force for advective heat removal is thermal convection, enhanced by the buoyancy of heated fluids. Convection has been already proposed by several authors as an important mechanism in the upper portion of a crustal detachment [*Kerrich and Hyndman*, 1986; *Losh*, 1997; *Manatschal et al.*, 2000], providing a good explanation to the downward and upward fluid movements indicated by oxygen isotopes shift and quartz veins precipitation. Our results further suggest that thermal convection was already effective at depth of late ductile deformation regime (quartz-calcite 3). For thermal convection to occur high permeabilities are required. These were provided during the veining stages V2a and especially V2b by vein density increase and interconnection (Figures 4, 5c, 5d, and 6). The size and location of convection cells can also be discussed. *Losh* [1997] has proposed that convection involve the whole upper crust over the detachment discontinuity. Published data from *Katzir et al.* [1996] rather suggest that the upper unit was not pervasively affected by ^{18}O alteration outside of a 60–80 m channel parallel to the contact discontinuity. Considering the distance of penetration of δ^{18}O alteration in the lower and upper units, one should thus consider the whole shear zone as a 100–150-m-thick tilted porous layer, in which convection cells occur at the scale of hundreds meters. The relay of convection cells is capable of transporting large quantities of heat by advection [*Criss and Hofmeister*, 1991].

[42] The above results strongly suggest that the detachment of Tinos, though representing a permeability barrier, was at least transiently infiltrated by surface-derived fluids until early ductile greenschist facies depth, and maybe down to blueschist facies. Similar conclusions were reached by *Fricke et al.* [1992] in the Ruby Mountain detachment. These authors suggested that dilatancy pumping triggers the downward infiltration of fluid into the ductile crust. Other independent studies of Basin and Range detachments, lacking a continuous record of δ^{18}O evolution, have interpreted veining and ^{18}O alteration as the result of two separate fluid systems, meteoric in the hanging wall and igneous in the footwall [*Kerrich and Rehrig*, 1987; *Morrison*, 1994; *Reynolds and Lister*, 1987]. Their data could as well be interpreted as the result of progressive increasing interaction with meteoric fluids as the shear zone opens to circulation.

6.5. Interpretation: Role of Large-Scale Fluid Infiltration in Detachment Evolution

[43] If widespread, the involvement of meteoric fluids below the ductile-to-brittle transition of shear zones could have important mechanical consequences on the initiation of crustal detachments. Since crustal strength is maximum at about the depth of the ductile-to-brittle transition [*Brace and Kohlstedt*, 1980], normal faults form at shallow level even though the strongest region of the middle crust is still deforming elastically. Normal faulting thus predates crustal failure and detachment formation [*Axen*, 1992; *Lister and Davis*, 1989]. Active normal faults reaching depth of at least 10 km are known to occur in context of continental extension [*Laigle et al.*, 2000], and to act as pathways for fluid migration. It is thus reasonable to assess that surface-derived fluids are already present at the base of the faulted brittle crust at the onset of continental rifting.

[44] Rheological studies have shown that the presence of fluids at midcrustal conditions can greatly alter the strength envelope of rocks, either by increasing the pore pressure [*Rice*, 1992] or by producing weak phyllosilicates during alteration reactions [*Bos and Spiers*, 2002; *Wintsch et al.*,

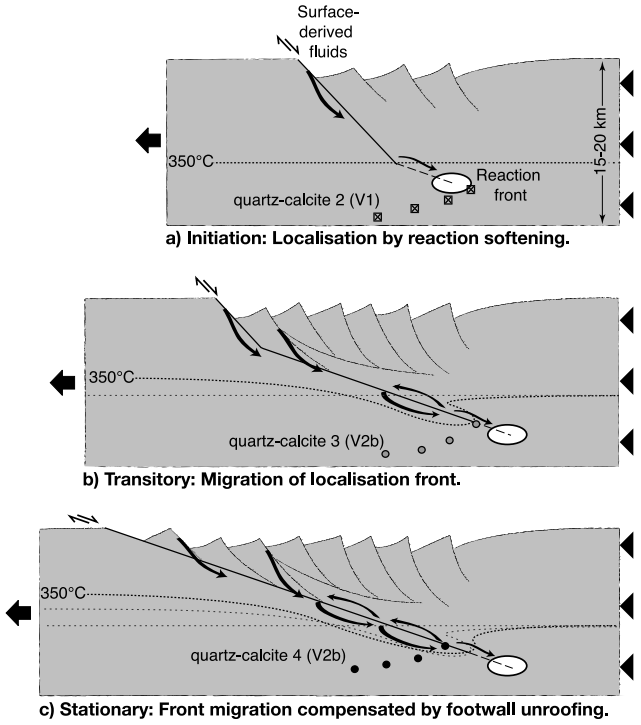

Figure 13. Cartoon showing a conceptual model of detachment evolution with infiltration of surface-derived fluids. (a) Downward flow through crustal fault, and localization of deformation along a low-angle plane initiated by reaction softening at the base of brittle crust. Quartz-calcite generation 1 in V1 veins is at the base of the reaction front. (b) Lowering of isotherms by advective cooling along convection cells in transitory state, and subsequent downward migration of the reaction front. Quartz-calcite 2 (V2a) occurs in ductile context after localization. (c) Evolution toward a stationary state: The downward migration of isotherms and the reaction front is compensated by the uplift of the footwall, as the rate of localization is equilibrated by the rate of opening. Quartz-calcite 3 and 4 (V2b) occur in late ductile-early brittle deformation, as convection cells disturb the thermal regime.

1995]. *Gueydan et al.* [2003] have recently used such a reaction softening process to propose a model of crustal strain localization promoted by fluid addition, leading to the nucleation of a low-angle shear zone at 10–15 km depth.

[45] In agreement with these recent advances, we thus propose an interpretation of detachment evolution, in which predetachment fluid infiltration acts as the destabilizing factor leading to strain localization (Figure 13). Fluids are driven to 10–15 km by large-scale normal faults, reaching the transitional depth between frictional and viscous regimes. Addition of surface-derived fluids at the base of the brittle crust promotes stress-induced hydration reactions beneath the tip of the fault in the ductile context (Figure 13a), yielding the formation of a shear zone by strain localization. At this early stage, only diffuse and nonlocalized penetration of fluids is expected, the composition of which is partially buffered by the wall rock at the hydration reaction front. This stage would correspond to generation 2 quartz and calcite (V2a stage) occurring in quasiplastic regime during the greenschist facies retrogression. As fluids infiltrate the newly formed shear zone section, the reaction front moves downward toward greater depth (Figure 13b). Thermal convection cells are established at and above the ductile-to-brittle transition, removing heat from the footwall. Quartz-calcite 3 (V2b), would crystallize at this stage, beneath the transition. As the footwall moves upward and enters the frictional sliding regime, fractures nucleate and connect, thus increasing the permeability. Veins at this stage are marked by a strong surface-derived fluid signature and steep temperature gradients (quartz-calcite 3 and 4, V2b veins, Figure 13c). As water is consumed by hydration reactions, surface-derived fluid infiltration recharges the convection system. Finally, the evolution of detachment production is expected to reach a stationary state. The downward propagation of the 350°C isotherm with fluids is compensated by the upward movement of the footwall, so that the reaction front stays at midcrustal depth (Figure 13c).

[46] The following consequences of the above model should be expected in regions of active extensional detachments: (1) Microseismicity should not be spread out homogeneously along the detachment, but localized in swarms of microseisms at or above the reaction front, in the continuation of normal faults rooting on the detachment. (2) The extensional movement accommodated by the advance of reaction fronts progressively forming low-angle planes should be directly proportional to the amount of heat extracted by fluid circulation.

[47] Indeed, *Rigo et al.* [1996] reported a shallow-dipping planar structure defined by the focuses of microseisms at 9–13 km beneath the gulf of Corinth, which they interpreted as a flat-lying detachment. They also noted that seisms were localized in swarms in the downward continuation of extensional faults, branching on the flat-lying structure. These swarms of seisms may represent reaction fronts. Besides, ODP Leg 180 borehole temperature measurements at Site 1108 revealed a thermal gradient of 100°C km^{-1} in the hanging wall of an active detachment fault in Woodlark Basin (Papua New Guinea). This temperature gradient was interpreted by *Floyd et al.* [2001] as convective heat transport by fluid flow along the detachment channel. Woodlark Basin is also characterized by an extremely fast opening rate in its continental portion (25-40 mm yr^{-1}) [*Taylor et al.*, 1999].

[48] There is increasing evidence that fluid flow plays a first order role in structural, geochemical, thermal, seismological, and mechanical aspects of detachment processes. Our tentative model, although speculative, would help to reconcile these independent observations, from the initiation of a detachment to the final stage of core complex exhumation.

7. Conclusions

[49] The core complex of Tinos Island has been intensely reworked by deformation and fluid interactions during its exhumation along a major shear zone. Careful description of finite strain patterns allowed us to recognize three types of metamorphic veins witnessing the complex interplay be-

tween fluid and deformation, as the ductile shear zone was transformed into a brittle detachment fault. The first type (V1 veins) formed in the deep root of the shear zone. V2 veins occurred at the transitional depth between ductile and brittle regimes. The third type (V3 veins) opened in the brittle crust. Detailed structural, cathodoluminescence an $\delta^{18}O$ ion microprobe analyses on mineral infilling these veins indicate that (1) The conductive thermal gradient of the footwall was disturbed by advective removal of heat along the detachment, probably by thermal convection. The ''footwall refrigeration'' proposed by Morrison and Anderson on a Californian detachment might be a widespread phenomenon. (2) This refrigeration was promoted by massive infiltration of surface-derived fluids over depths of 10–15 km. (3) Massive fluid fluxes occurred with the coalescence of late ductile-early brittle veins, as the exhuming footwall crossed the ductile-brittle transition. (4) Only small amounts of fluids penetrated the ductile crust beneath the transitional rheology.

[50] Our results on the infiltration of surface-derived fluids support recent advances in shear zone modeling, showing that fluid inputs in the faulted crust may yield to strain localization by reaction softening. Brittle fault networks at the onset of rifting, by supplying fluids to the ductile-to-brittle transition would thus play a key role in the nucleation of a crustal detachment. This interpretation needs to be confirmed by independent results from active extensional detachment regions, combining heat flow measurements, fluid flow balance and microseismicity inversion along deep-seated normal faults.

Appendix A

[51] The empirical calibration between the temperature T and the quartz-calcite fractionation Δ_{Qz-Cc} of *Sharp and Kirschner* [1994] is

$$\Delta_{Qz-Cc} = A.10^6/T^2$$

with $A = 0.78$. In this study, the total 1 standard deviation error on temperature σ_T was therefore calculated as

$$\sigma_T^2 = \sigma_A^2(\partial T/\partial A)^2 + \sigma_{\Delta_{Qz-Cc}}^2\left(\partial T/\partial \Delta_{Qz-Cc}\right)^2,$$

where $\sigma_A = 0.08$ is the uncertainty on A, and $\sigma_{\Delta_{Qz-Cc}}$ is the error on Δ_{Qz-Cc}, given by the total 1 standard deviation uncertainty on each of the two $\delta^{18}O$ measurements in quartz and calcite (total 1 standard deviation uncertainty is taken as the sum of the analytical precision of the $\delta^{18}O$ measurement, limited by the internal error due to counting statistics, and the accuracy on the determination of the IMFs, limited by the external reproducibility on standards).

[52] In a same way, the empirical calibrations between mineral-water fractionations and the temperature are defined as

$$\Delta_{\text{mineral}-H_2O} = C_1.10^6T^2 + C_2.10^3T + C_3,$$

where C_1, C_2, C_3 are the coefficients of the calcite-water and quartz-water calibrations. The total 1 standard deviation error on the O isotopic composition of water $\sigma_{\partial^{18}O_{H_2O}}$ was therefore calculated as

$$\begin{aligned}\sigma_{\partial^{18}O_{H_2O}} = {} & \sigma_{C_1}^2\left(\partial\partial^{18}O_{H_2O}/\partial C_1\right)^2 + \sigma_{C_2}^2\left(\partial\partial^{18}O_{H_2O}/\partial C_2\right)^2 \\ & + \sigma_{C_3}^2\left(\partial\partial^{18}O_{H_2O}/\partial C_3\right)^2 + \sigma_T^2\left(\partial\partial^{18}O_{H_2O}/\partial T\right)^2 \\ & + \sigma_{\partial^{18}O_{\text{mineral}}}^2\end{aligned}$$

Since C_1, C_2 and C_3 are very well constrained for the calcite-H_2O equilibrium in the temperature range 100°–500°C, the uncertainties σ_{Ci} can be neglected [*Sharp and Kirschner*, 1994; *Zheng*, 1999]. The σ_{C1} and σ_{C3} were taken equal to 0.08 for the quartz-H_2O equilibrium ($C_2 = 0$ as given by *Sharp and Kirschner* [1994]). Consequently, the error on the $\delta^{18}O_{H2O}$ from quartz is slightly higher that of the $\delta^{18}O_{H2O}$ from calcite in Table 2.

[53] **Acknowledgments.** The authors wish to acknowledge Marc Chaussidon, Michel Champenois, and Etienne Deloule for conducting the tuning and data acquisition at the ion microprobe of the CRPG-CNRS of Nancy. Mihai Ducea, Jean Morrison, and Steven Losh are thanked for their insightful comments and suggestions that improved the earlier version of this manuscript. This work was supported by INSU-CNRS and CEPAGE grants.

References

Aléon, J., M. Chaussidon, B. Marty, L. Schütz, and R. Jaenicke (2002), Oxygen isotopes in single micrometer-sized quartz grains: Tracing the source of Saharan dust over long-distance atmospheric transport, *Geochim. Cosmochim. Acta*, *66*, 3351–3365.

Altherr, R., H. Kreuzer, I. Wendt, H. Lenz, G. A. Wagner, J. Keller, W. Harre, and A. Höhndorf (1982), A late Oligocene/early Miocene high temperature belt in the Attic-Cycladic Crystalline Complex (SE Pelagonian Greece), *Geol. Jahrb. Reihe E*, *23*, 97–164.

Altherr, R., F. Henjes-Kunst, A. Matthews, H. Friedrichsen, and B. T. Hansen (1988), O-Sr isotopic variations in Miocene granitoids from the Aegean: Evidence for an origin by combined assimilation and fractional crystallization, *Contrib. Mineral. Petrol.*, *100*, 528–541.

Angelier, J., N. Lybéris, X. Le Pichon, E. Barrier, and P. Huchon (1982), The tectonic development of the Hellenic Arc and the Sea of Crete: A synthesis, *Tectonophysics*, *86*, 159–196.

Avigad, D., and Z. Garfunkel (1989), Low-angle faults above and below a blueschist belt: Tinos Island, Cyclades, Greece, *Terra Nova*, *1*, 182–187.

Avigad, D., and Z. Garfunkel (1991), Uplift and exhumation of high-pressure metamorphic terranes: The example of the Cycladic blueschist belt (Aegean Sea), *Tectonophysics*, *188*, 357–372.

Axen, G. (1992), Pore pressure, stress increase, and fault weakening in low-angle normal faulting, *J. Geophys. Res.*, *97*, 8979–8991.

Axen, G., J. Selverstone, and T. Wawrzyniec (2001), High-temperature embrittlement of extensional Alpine mylonite zones in the midcrustal ductile-brittle transition, *J. Geophys. Res.*, *106*, 4337–4347.

Bertotti, G., and M. ter Voorde (1994), Thermal effect of normal faulting during rifted basin formation, 2. The Lugano-Val Grande normal fault and the role of pre-existing thermal anomalies, *Tectonophysics*, *240*, 145–157.

Bonneau, M., and J. R. Kienast (1982), Subduction, collision et schistes bleus: L'exemple de l'Egée (Grèce), *Bul. Soc. Geol. Fr.*, *7*, 785–791.

Bos, B., and C. Spiers (2002), Frictional-viscous flow of phyllosilicate-bearing fault rock: Microphysical model and implications for crustal strength profiles, *J. Geophys. Res.*, *107*(B2), 2028, doi:10.1029/2001JB000301.

Brace, W. F., and D. L. Kohlstedt (1980), Limits on lithospheric stress imposed by laboratory experiments, *J. Geophys. Res.*, *85*, 6248–6252.

Bröcker, M. (1990), Blueschist-to-greenschist transition in metabasites from Tinos Island, Cyclades, Greece: Compositional control or fluid infiltration?, *Lithos*, *25*, 25–39.

Bröcker, M., and L. Franz (1998), Rb-Sr isotope studies on Tinos Island (Cyclades, Greece): Additional time constraints for metamorphism, extent of infiltration-controlled overprinting and deformational activity, *Geol. Mag.*, *135*(3), 369–382.

Bröcker, M., H. Kreuzer, A. Matthews, and M. Okrusch (1993), $^{40}Ar/^{39}Ar$ and oxygen isotope studies of polymetamorphism from Tinos Island, Cycladic blueschist belt, Greece, *J. Metamorph. Geol.*, *11*, 223–240.

Burkhard, M. (1993), Calcite twins, their geometry, appearance and significance as stress-strain markers and indicators of tectonic regime: A review, *J. Struct. Geol.*, *15*, 351–368.

Criss, R. E., and A. M. Hofmeister (1991), Application of fluid dynamics principles in tilted permeable media to terrestrial hydrothermal systems, *Geophys. Res. Lett.*, *18*, 199–202.

Dinter, D. A., and L. Royden (1993), Late Cenozoic extension in north-eastern Greece: Strymon Valley detachment system and Rhodope metamorphic core complex, *Geology*, *21*, 45–48.

Dipple, G. M., R. P. Wintsch, and S. Andrews (1990), Identification of the scales of differential element mobility in a ductile fault zone, *J. Metamorph. Geol.*, *8*, 645–661.

Dürr, S., R. Altherr, J. Keller, M. Okrusch, and E. Seidel (1978), The median Aegean crystalline belt: Stratigraphy, structure, metamorphism, magmatism, in *Alps, Appenines, Hellenides*, *Inter-Union Comm. Geodyn. Sci. Rep. 38*, edited by H. Closs, D. Roeder, and K. Schmidt, pp. 455–477, Schweizerbart, Stuttgart, Germany.

Etheridge, M. A., V. J. Wall, and R. H. Vernon (1983), The role of the fluid phase during regional metamorphism and deformation, *J. Metamorph. Geol.*, *1*, 205–226.

Famin, V., P. Philippot, and L. Jolivet (2000), Nature et rôle des fluides dans la localisation de la déformation, lors de l'exhumation d'un domaine métamorphique, paper presented at Réunion des sciences de la Terre (RST 2000), Soc. Geol. de Fr., Paris, France.

Famin, V., S. Nakashima, L. Jolivet, and P. Philippot (2004), Mobility of metamorphic fluids inferred from Infrared microspectroscopy on natural fluid-inclusions: The example of Tinos Island (Cyclades Greece), *Contrib. Mineral. Petrol.*, *146*, 736–749.

Farver, J. R. (1990), Oxygen self-diffusion in calcite: Dependence on temperature and water fugacity, *Eos Trans. AGU*, *71*, 1655.

Farver, J. R., and R. A. Yund (1991), Oxygen diffusion in quartz: Dependence on temperature and water fugacity, *Chem. Geol.*, *90*, 55–70.

Faure, M., M. Bonneau, and J. Pons (1991), Ductile deformation and syntectonic granite emplacement during the late Miocene extension of the Aegea (Greece), *Bull. Soc. Geol. Fr.*, *162*, 3–11.

Fisler, D. K., and R. T. Cygan (1999), Diffusion of Ca and Mg in calcite, *Am. Mineral.*, *84*, 1392–1399.

Floyd, J. S., J. C. Mutter, A. M. Goodlife, and B. Taylor (2001), Evidence for fault weakness and fluid flow within an active low-angle normal fault, *Nature*, *411*, 779–783.

Fricke, H. C., S. M. Wickham, and J. R. O'Neil (1992), Oxygen and hydrogen isotope evidence for meteoric water infiltration during mylonitization and uplift in the Ruby Mountains-East Humboldt Range core complex, Nevada, *Contrib. Mineral. Petrol.*, *111*, 203–221.

Ganor, J., A. Matthews, and N. Paldor (1991), Diffusional isotopic exchange across an interlayered marble-schist sequence with an application to Tinos, Cyclades, Greece, *J. Geophys. Res.*, *96*, 18,073–18,080.

Ganor, J., A. Matthews, and M. Schliestedt (1994), Post-metamorphic low $\delta^{13}C$ calcite in the Cycladic complex (Greece) and their implications for modeling fluid infiltration processes using carbon isotope compositions, *Eur. J. Mineral.*, *4*, 365–379.

Ganor, J., A. Matthews, and M. Schliestedt (1996), Oxygen isotopic heterogeneities of metamorphic rocks: An original tectonostratigraphic signature, or an imprint of exotic fluids?: A case study of Sifnos and Tinos islands (Greece), *Eur. J. Mineral.*, *8, 719–732.*

Gautier, P., and J. P. Brun (1994a), Crustal-scale geometry and kinematics of late-orogenic extension in the central Aegean (Cyclades and Evvia Islands), *Tectonophysics*, *238*, 399–424.

Gautier, P., and J. P. Brun (1994b), Ductile crust exhumation and extensional detachments in the central Aegean (Cyclades and Evvia Islands), *Geodyn. Acta*, *7*, 57–85.

Graham, C. M., J. Valley, and B. M. Winter (1996), Ion microprobe analysis of $^{18}O/^{16}O$ in authigenic and detrital quartz in the St. Peter Sandstone, Michigan basin and Wisconsin Arch, USA: Contrasting diagenetic histories, *Geochim. Cosmochim. Acta*, *60*, 5101–5116.

Gueydan, F., Y. M. Leroy, L. Jolivet, and P. Agard (2003), Analysis of continental midcrustal strain localization induced by microfracturing and reaction-softening, *J. Geophys. Res.*, *108*(B2), 2064, doi:10.1029/2001JB000611.

Jolivet, L., and M. Patriat (1999), Ductile extension and the formation of the Aegean sea, in *The Mediterranean Basins: Tertiary Extension Within the Alpine Orogen*, edited by B. Durand et al., *Geol. Soc. Spec. Publ.*, *156*, 427–456.

Jolivet, L., J.-P. Brun, P. Gautier, S. Lallemant, and M. Patriat (1994), 3-D kinematics of extension in he Aegean region from the early Miocene to the present, insights from the ductile crust, *Bull. Soc. Geol. Fr.*, *165*, 195–209.

Katzir, Y., A. Matthews, Z. Garfunkel, M. Schliestedt, and D. Avigad (1996), The tectono-metamorphic evolution of a dismembered ophiolite (Tinos Cyclades, Greece), *Geol. Mag.*, *133*, 237–254.

Kerrich, R., and R. D. Hyndman (1986), Thermal and fluid regimes in the Bitterroot lobe-Sapphire block detachment zone, Montana: Evidence from $^{18}O/^{16}O$ and geologic relations, *Geol. Soc. Am. Bull.*, *97*, 147–155.

Kerrich, R., and W. Rehrig (1987), Fluid motion associated with Tertiary mylonitization and detachment faulting: $^{18}O/^{16}O$ evidence from the Picacho metamorphic core complex, Arizona, *Geology*, *15*, 58–62.

Kerrich, R., T. E. La Tour, and L. Willmore (1984), Fluid participation in deep fault zones: Evidence from geological, geochemical and $^{18}O/^{16}O$ relations, *J. Geophys. Res.*, *88*, 4331–4343.

Laigle, M., A. Hirn, M. Sachpazi, and N. Roussos (2000), North Aegean crustal deformation: An active fault imaged to 10 km depth by reflection seismic data, *Geology*, *28*, 71–74.

Lee, J., and G. S. Lister (1992), Late Miocene ductile extension and detachment faulting, Mykonos, Greece, *Geology*, *20*, 121–124.

Le Pichon, X., N. Chamot-Rooke, and S. Lallemant (1995), Geodetic determination of the kinematics of central Greece with respect to Europe: Implications for eastern Mediterranean tectonics, *J. Geophys. Res.*, *100*, 12,675–12,690.

Lister, G. S., and G. A. Davis (1989), The origin of metamorphic core complexes and detachment faults formed during the Tertiary continental extension in the northern Colorado River region, *J. Struct. Geol.*, *11*, 65–94.

Lister, G. S., G. Banga, and A. Feenstra (1984), Metamorphic core complexes of Cordilleran type in the Cyclades, Aegean Sea, Greece, *Geology*, *12*, 221–225.

Losh, S. (1997), Stable isotope and modeling studies of fluid-rock interaction associated with the Snake Range and Mormon Peak detachment faults, Nevada, *Geol. Soc. Am. Bull.*, *109*, 300–323.

Manatschal, G., D. Marquer, and G. Früh-Green (2000), Channelized fluid flow and mass transfer along a rift-related detachment fault (Eastern Alps, southern Switzerland), *Geol. Soc. Am. Bull.*, *112*, 21–33.

Mancktelow, N. S., and B. Grasemann (1997), Time-dependent effects of heat advection and topography on cooling histories during erosion, *Tectonophysics*, *270*, 167–195.

Matthews, A., J. Lieberman, D. Avigad, and Z. Garfunkel (1999), Fluid-rock interaction and thermal evolution during thrusting of an Alpine metamorphic complex (Tinos Island Greece), *Contrib. Mineral. Petrol.*, *135*, 212–224.

McCaig, A. M. (1988), Deep fluid circulation in fault zones, *Geology*, *16*, 867–870.

McKenzie, D. (1972), Active tectonics of the Mediterranean region, *Geophys. J. Astron. Soc.*, *30*, 109–185.

Mélidonis, N. G. (1980), The geological structure and mineral deposits of Tinos Island (Cyclades Greece), *Geol.*, 1–80.

Morrison, J. (1994), Meteoric water-rock interaction in the lower plate of the Whipple Mountain metamorphic core complex, California, *J. Metamorphic Geology*, *12*, 827–840.

Morrison, J., and J. L. Anderson (1998), Footwall refrigeration along a detachment fault: Implications for the thermal evolution of core complexes, *Science*, *279*, 63–66.

Parra, T., O. Vidal, and L. Jolivet (2002), Relation between deformation and retrogression in blueschist metapelites of Tinos Island (Greece) evidenced by chlorite-mica local equilibria, *Lithos*, *63*, 41–66.

Patzak, M., M. Okrusch, and H. Kreuzer (1994), The Akrotiri Unit on the Island of Tinos, Cyclades, Greece: Witness to a lost terrane of late Cretaceous age, *Neues Jahrb. Geol. Paleontol. Abh.*, *194*, 211–252.

Peters, M. T., and S. M. Wickham (1995), On the causes of ^{18}O-depletion and $^{18}O/^{16}O$ homogenization during regional metamorphism: The East Humboldt Range core complex, Nevada, *Contrib. Mineral. Petrol.*, *119*, 68–82.

Reynolds, S. J., and G. S. Lister (1987), Structural aspects of fluid-rock interactions in detachment zones, *Geology*, *15*, 362–366.

Rice, J. (1992), Fault stress states, pore pressure distributions, and the weakness of San Andreas fault, in *Fault Mechanics and Transport Properties of Rocks: A Festschrift in Honor of W.F. Brace*, edited by B. Evans and T. F. Wong, pp. 475–503, Academic, San Diego, Calif.

Rigo, A., H. Lyon-Caen, R. Armijo, A. Deschamps, D. Hatzfeld, K. Makropoulos, P. Papadimitriou, and I. Kassaras (1996), A microseismicity study in the western part of the Gulf of Corinth (Greece): implications for large-scale normal faulting mechanisms, *Geophys. J. Int.*, *126*, 663–688.

Roberts, S., D. J. Sanderson, and P. Gumiel (1999), Fractal analysis and percolation properties of veins, in *Fractures, Fluid Flow and Mineralization*, edited by K. J. W. McCaffrey, L. Lonergan, and J. J. Wilkinson, *Geol. Soc. Spec. Publ.*, *155*, 7–16.

Rollion-Bard, C., M. Chaussidon, and C. France-Lanord (2003), pH control on oxygen isotopic composition of symbiotic corals, *Earth Planet. Sci. Lett.*, *215*, 275–288.

Sharp, Z. D., and D. L. Kirschner (1994), Quartz-calcite oxygen isotope thermometry: A calibration based on natural isotopic variations, *Geochim. Cosmochim. Acta*, *58*, 4491–4501.

Sheppard, S. M. F. (1986), Characterization and isotopic variations in natural waters, in *Stable Isotopes in High Temperature Geological Processes, Rev. Mineral.*, vol. 16, edited by J. W. Valley, M. P. Taylor, and J. R. O'Neil, Mineral. Soc. of Am., Washington, D.C.

Sokoutis, D., J. P. Brun, J. V. D. Driessche, and S. Pavlides (1993), A major Oligo-Miocene detachment in southern Rhodope controlling north Aegean extension, *J. Geol. Soc. London*, *150*, 243–246.

Taylor, B., A. M. Goodlife, and F. Martinez (1999), How continents break up: Insights from Papua New Guinea, *J. Geophys. Res.*, *104*, 7497–7512.

Wintsch, R. P., R. Christoffersen, and A. K. Kronenberg (1995), Fluid-rock reaction weakening of fault zones, *J. Geophys. Res.*, *100*, 13,021–13,032.

Zheng, Y. F. (1999), Oxygen isotope fractionation in carbonate and sulfate minerals, *Geochem. J.*, *33*, 109–126.

P. Agard, V. Famin, and L. Jolivet, Laboratoire de Tectonique, Université Pierre et Marie Curie, case 129, 4 place Jussieu, F-75252 Paris Cedex 05, France. (vincent.famin@lgs.jussieu.fr)

P. Philippot, CNRS, Laboratoire de Géosciences Marines, Institut de Physique du Globe, case 89, Université Pierre et Marie Curie, 4 place Jussieu, F-75252 Paris Cedex 05, France.

Figure 7. Microstructures and $\delta^{18}O$ mapping in V1 and V2b veins, on the example of samples V1.1 and V2b.3, taken at 8 m under the detachment (images location in Figures 3b and 3f). (a) Optic imaging of generation 1 quartz and calcite in V1 vein (sample V1.1). (b) Cathodoluminescence (CL) imaging of Figure 7a, with corresponding temperatures around 350°C using $\delta^{18}O$ fractionation between quartz and calcite. (c) Optic imaging of generation 2 in V1 at 8 m under the contact (sample V1.1). (d) CL imaging of Figure 7c, with temperatures around 225°C. (e) Optic imaging of generation 3 quartz and calcite in V2b vein sampled at 8 m under the detachment (sample V2b.3). (f) CL imaging of Figure 7e, with temperature around 120°C. (g) Optic imaging of generation 4 in V2b at 8 m under the contact (sample V2b.3). (h) CL imaging of Figure 7g with $\delta^{18}O$ temperatures between 120° and 270°C.

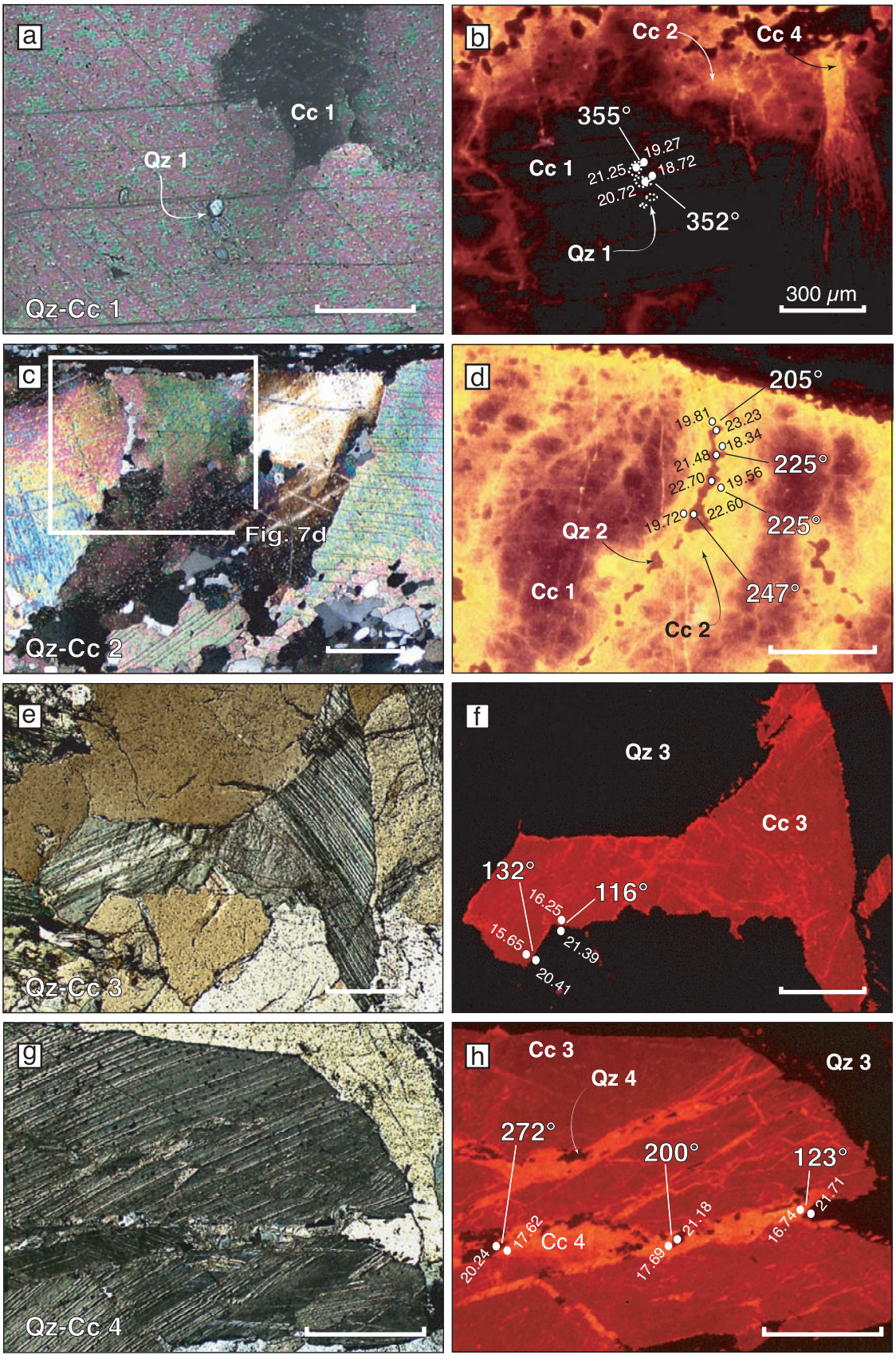
a
Cc 1
Qz 1
Qz-Cc 1
b
Cc 2
Cc 4
355°
19.27
Cc 1
21.25
18.72
20.72
352°
Qz 1
300 μm
c
Fig. 7d
Qz-Cc 2
d
205°
19.81
23.23
21.48
18.34
225°
22.70
19.56
19.720
22.60
225°
Qz 2
Cc 1
247°
Cc 2
e
Qz-Cc 3
f
Qz 3
Cc 3
132°
16.25
116°
15.65
21.39
20.41
g
Qz-Cc 4
h
Cc 3
Qz 4
Qz 3
272°
200°
123°
21.71
16.74
20.24
17.62
Cc 4
17.69
21.18

Figure 7